J. Fluid Mech. (2007), *vol.* 575, *pp.* 359–397. © 2007 Cambridge University Press
doi:10.1017/S002211200600440X Printed in the United Kingdom

Two-dimensional resonant piston-like sloshing in a moonpool

ODD M. FALTINSEN, OLAV F. ROGNEBAKKE AND ALEXANDER N. TIMOKHA

Centre for Ships and Ocean Structures, NTNU, N-7491 Trondheim, Norway

(Received 31 January 2006 and in revised form 23 September 2006)

This paper presents combined theoretical and experimental studies of the two-dimensional piston-like steady-state motions of a fluid in a moonpool formed by two rectangular hulls (e.g. a dual pontoon or catamaran). Vertical harmonic excitation of the partly submerged structure in calm water is assumed. A high-precision analytically oriented linear-potential-flow method, which captures the singular behaviour of the velocity potential at the corner points of the rectangular structure, is developed. The linear steady-state results are compared with new experimental data and show generally satisfactory agreement. The influence of vortex shedding has been evaluated by using the local discrete-vortex method of Graham (1980). It was shown to be small. Thus, the discrepancy between the theory and experiment may be related to the free-surface nonlinearity.

1. Introduction

'Moonpools' are vertical openings, through the deck and hull of ships or barges, used for marine and offshore operations such as pipe laying or diver recovery. The riser systems of drilling ships and of a few floating production storage and offloading (FPSO) ships pass through a moonpool. Being exposed to incident waves or harmonic ship motions, the fluid inside moonpools may perform considerable piston-like motions, i.e. vertical oscillations of the mean surface with amplitudes substantially larger than the vertical ship motions. Similar fluid behaviour may happen between the hulls of multi-hull vessels or between ships in a side-by-side arrangement. Treating this problem within the framework of the linearized theory of water waves (Molin 2001; McIver 2005; Kuznetsov, Maz'ya & Vainberg 2002), the fluid motions inside the moonpool demonstrate a resonance.

When the steady-state velocity potential is regarded as a function of the complex frequency, resonances may be related to a pole in the complex-frequency domain that lies close to the real frequency axis. For some geometries, the complex frequency may lie on the real axis. In this case, the spectral problem on standing waves satisfying the condition of zero-radiant waves has an eigenvalue. The eigenfunction which corresponds to the eigenvalue forms so-called 'trapping structures'. Resonant forcing of the trapped mode leads to localization of the averaged total energy near the ship. A consequence is that the linear resonant amplitude of the trapped mode becomes theoretically infinite. The possible existence of trapping and complex resonances for two-dimensional steady-state waves around two symmetric bodies in finite water depth was investigated by Kuznetsov, McIver & Linton (2001), Kuznetsov *et al.* (2002) and McIver (1996, 2005). The resonance due to trapped modes at a floating torus has

https://doi.org/10.1017/S002211200600440X Published online by Cambridge University Press

been studied by, for instance, Newman (1999). However, the existence of trapped modes is a rare exception for actual moonpools including, most probably, our studied case of two equal-sized free-surface-piercing horizontal rectangular cylinders (see the computational results of Williams & Abul-Azm (1997) and Drobyshevski (2004), and references therein). Calculations and experiments by Ohkusu (1970) and Ohkusu & Takaki (1971), which were devoted to waves excited by forced harmonic vertical oscillations of two semi-submerged horizontal circular cylinders, also failed to reveal a trapped mode.

A quasi-analytical approximation of the resonant frequencies and corresponding modes for a rectangular moonpool in a two-dimensional barge was analysed by Molin (2001) in a simple and ingenious way. In order to get a symmetric approximate eigenvalue problem, he assumed that the beam of the barge is much larger than the width of the moonpool. To mimic the effect of the outer free surface, Molin (2001) located two sinks symmetrically on the horizontal axis (at keel level), at distances $\pm b_*/2$ from the barge centre (b_* is somewhat larger than the beam of the barge; speculative manipulations with these distances were described by Maisondieu *et al.* (2001)), so that, owing to the harmonicity of the inflow–outflow through the sinks, the integral mass flux at any instant, through the free surface and into the sinks, is zero. This approach is, however, hardly applicable for the description of resonant waves. A reason is that the existence of outgoing waves, even if they are small, causes a phase shift of the fluid motions inside the moonpool relative to the forced motion. The phase shift changes with the excitation frequency. However, Molin's eigenvalue approximation is not able to identify this phase shift.

Focusing on the radiation problem (there are no incident waves) and vertical (heave) excitations of the rectangular structure, the present paper studies two-dimensional resonant piston-like motions inside the moonpool for finite water depth. The smallness of the forcing amplitude is postulated. The resonance conditions at an isolated forcing frequency are associated with a local peak in the steady-state amplitude of the piston-like mode. The first goal of the paper consists of obtaining a precise analytical approximation of the linearized surface-wave problem that can be used as a basis in analytically oriented asymptotic studies of nonlinear resonant motions, as in the works by Faltinsen (1974) and Faltinsen *et al.* (2000), which were devoted to sloshing motions in two-dimensional rectangular tanks. The second goal of the paper is to study the effect of vortex shedding. The third goal consists of performing model tests on the steady-state forced-wave amplitudes for piston-like regimes in order to validate the theoretical results.

Our method is based on the domain-decomposition scheme, which leads to a system of integral equations on the transmission interfaces (see the papers Mavrakos 2004; Drobyshevski 2004; Kuznetsov *et al.* 2002, and references therein). After a mathematical statement of the problem in § 2, we introduce the Neumann traces along the transmission interfaces and use an integral representation for the corresponding inhomogeneous boundary-value problems (the kernels of the integral representations may be treated as Green functions of a special type; see Courant & Hilbert 1953, chapter 5, § 14). The Dirichlet (pressure) transmission conditions are employed to derive a system of linear integral equations (§ 3.1.4) governing the Neumann traces. The integral equations are in part similar to the results of Porter & Evans (1995) and Kuznetsov *et al.* (2001). In §§ 3.2.1 and 3.2.2, the integral system is solved by the Galerkin method of adopting a special basis which captures the actual singularities at the corner points of rectangular hulls. A similar technique for other surface-wave problems was presented by Porter & Evans (1995) and Gavrilyuk *et al.* (2006).

https://doi.org/10.1017/S002211200600440X Published online by Cambridge University Press

Further, this basis system facilitates the derivation of analytical expressions for the elements of the matrix problem which appears in the Galerkin method. As a result, the approximate solution guarantees fast convergence and provides from six to eight significant figures with only six to nine basis functions on each transmission interface. An accurate prediction of the singularities at the corners is needed to capture the vortex-shedding effect. This is done by combining our projective method with the discrete-vortex method of Graham (1980) and Downie, Bearman & Graham (1988). The original radiation problem is not solvable for a given forcing frequency only when there exists a trapped-mode solution (see, for instance, Kuznetsov *et al.* 2002; McIver, McIver & Zhang 2003; McIver 2005); if this is not the case then both integral and approximate (matrix) problems have a unique solution. In § 3.3 we show that, in an approximate sense, the resonance behaviour for any given dimensionless forcing frequency may be related to the zeroes in the determinant of a submatrix.

In § 4 we describe the model tests and compare the linear predictions of resonant steady-state motions with experimental data. An emphasis is placed on the theoretical and experimental values of the resonant frequency as well as on a quantitative comparative analysis of both the piston-like elevations and also the wave amplitudes in the far field (§§ 4.2.1–4.2.2). In the experimental sense, resonances are related to the non-dimensional frequencies at which a local maximum for the piston-like amplitude occurs. Also in § 4.2.2, and in § 4.2.3, we study the added-mass and damping coefficients as functions of the forcing frequency for all the experimental cases. Finally, asymptotic solutions as the forcing frequency vanishes, as well as the corresponding finite limit for the damping coefficient, are derived. The comparative analysis shows that the theoretical resonant frequencies (§ 4.2.1) are in reasonable agreement with experiment for smaller forcing amplitudes. However, the discrepancy increases for larger excitations and for wider mooonpools. Section 4.2.2 gives a systematic comparative analysis and discusses the discrepancy. Two types of nonlinearity, namely, free-surface nonlinearity and vortex shedding at the corners, should be accounted for to remove the discrepancy. An intuitive reason for the presence of the free-surface nonlinearity is the observed narrowing of the resonance zone and jump-like behaviour occurring at isolated frequencies on the experimental response curves. Nonlinear analyses by Vinje (1991) for the limiting case of a moonpool of narrow opening, by Miles (2004) for a one-dimensional model of piston-like motions in a well by Hirata & Craik (2003) for the simplest possible equivalent mechanical model indicate that the free-surface nonlinearity may matter. In the case of a wider moonpool, the discrepancy may also be related to a complex interaction between the piston-like mode and a sloshing mode. The latter refers to the secondary resonance in the system (see the discussion of complications due to secondary resonance in sloshing problems by Faltinsen & Timokha (2001)).

Because vortex shedding is one possible reason for a decrease in the maximum piston-like wave amplitude with increasing forcing amplitude, a local discrete vortex method as described by Graham (1980) and Downie *et al.* (1988) is applied. In § 5, we derive an explicit formula for the vortex-induced vertical force on the side hulls in terms of the coefficients of the singular functions used in the Galerkin basis. An important assumption of the local-discrete-vortex method is that the shed vorticity remains in a small vicinity of the hull corners. Our analysis assumes steady-state conditions, with the consequence that vorticity of equal magnitude but different signs is generated in two subsequent semicycles. The experimental and numerical study by Maisondieu *et al.* (2001) and some of the results of Molin *et al.* (2002) are relevant for our studies in § 5. However, there are important differences. Maisondieu *et al.*

https://doi.org/10.1017/S002211200600440X Published online by Cambridge University Press

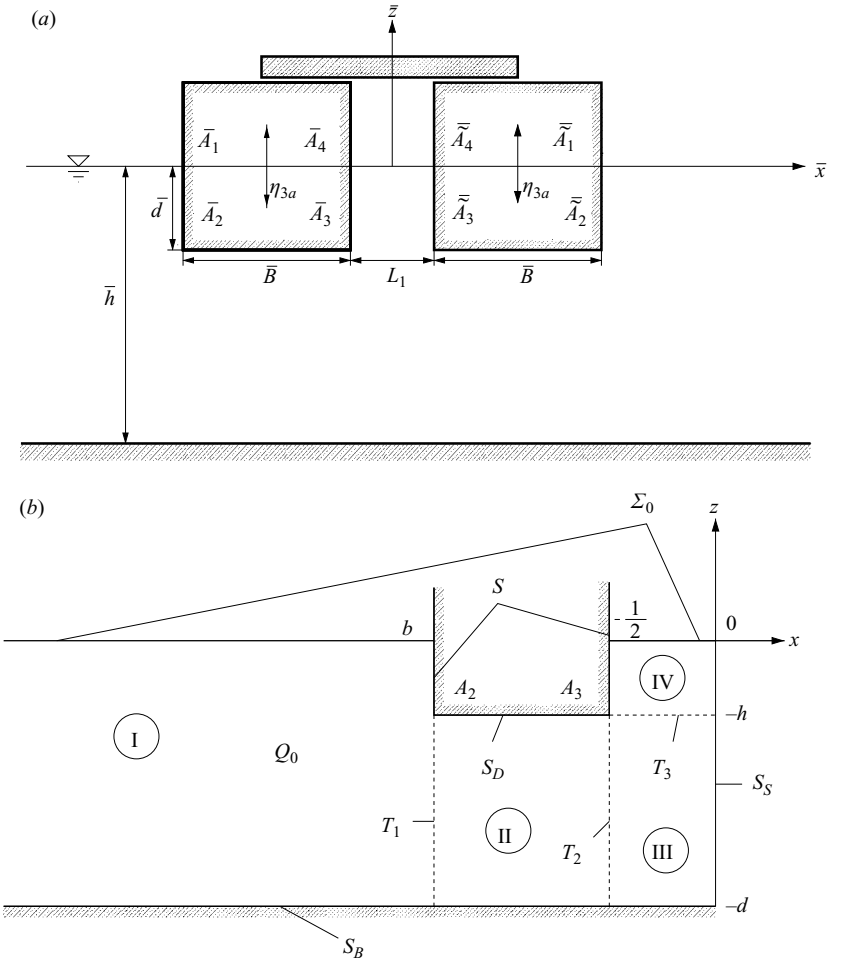


FIGURE 1. (*a*) General geometric sketch and (*b*) notation for the dimensionless problem.

(2001) considered free oscillations, with, in general, a significantly larger initial water elevation than our maximum piston-like amplitude, in steady-state regimes. They showed that in the initial phase until the motion is small there is a clear damping effect on the moonpool flow that cannot be described by wave radiation. Our numerical results based on the local vortex method demonstrate that this additional vortex-induced force gives only a very small contribution to the damping coefficient (the amplitude of the outgoing waves) for our experimental cases. A reason is that it is a second-order effect and all the excitation amplitudes are relatively small. It is also possible that a large vortex was generated in the test of Maisondieu *et al.* (2001). The vortex may have remained for a long time and not have been totally counteracted by vorticity shed later; this can occur for steady-state regimes.

2. Statement of the problem

We study two-dimensional $O\bar{z}$-symmetric steady-state surface waves caused by small-amplitude vertical regular oscillatory motions of two rigidly connected rectangular hulls in a finite water depth, as shown in figure 1(*a*). The analysis suggests

https://doi.org/10.1017/S002211200600440X Published online by Cambridge University Press

a non-dimensional formulation, in which all the geometric dimensions are scaled by the horizontal width of the moonpool, L_1 (the distance between the hulls). The characteristic time is equal to $1/\sigma$, where σ is the forcing angular frequency. This implies a redefinition of the dimensional variables (which have overbars) in non-dimensional form as follows:

$$x = \bar{x}/L_1, \quad z = \bar{z}/L_1, \quad t = \sigma\bar{t}, \quad \Lambda = \frac{\sigma^2 L_1}{g}, \quad \psi(x,z,t) = \frac{1}{L_1^2\sigma}\bar{\psi}(\bar{x},\bar{z},\bar{t}), \tag{2.1}$$

where ψ is the non-dimensional velocity potential and g is the acceleration due to gravity. As a particular consequence, the distance between the rectangular body and the Oz-axis (the symmetry axis) becomes equal to 1/2, the scaled dimensions of the stationary immersed rectangular body are $d = \bar{d}/L_1$ in the vertical direction and $B = \bar{B}/L_1 = \bar{b}/L_1 - 1/2$ in the horizontal direction. The non-dimensional water depth is $h = \bar{h}/L_1$ and the non-dimensional forcing amplitude is $\epsilon = \eta_{3a}/L_1 \ll 1$, where the dimensional vertical motion of the moonpool is defined by $\eta_3(t) = -\eta_{3a}\cos\sigma t$. Because the piston-like steady-state sloshing inside the moonpool is described by Oz-symmetric solutions, the non-dimensional velocity potential is found in the left-hand semi-band ($x \leqslant 0$), as shown in figure 1(*b*).

As a rule, we use overbars to distinguish a dimensional variable from a non-dimensional variable. In particular, we denote by $\bar{A}_i$ and $\bar{\tilde{A}}_i$ the intersections of the water plane with the hulls ($i = 1, 4$) and the immersed edges, as shown in figure 1(*a*). The symbols for the same points in the non-dimensional case will not have overbars.

Assuming that $\nabla\psi \sim \epsilon \ll 1$ and neglecting the $o(\epsilon)$ terms, the following linearized problem for steady-state linear waves in the left-hand semi-band is formulated:

$$\Delta\psi = 0 \quad \text{in} \quad Q_0, \qquad \frac{\partial\psi}{\partial\nu} = 0 \quad \text{on} \quad S_B + S + S_S, \tag{2.2a}$$

$$\frac{\partial\psi}{\partial\nu} = \epsilon\sin t \quad \text{on} \quad S_D, \tag{2.2b}$$

$$\Lambda\frac{\partial^2\psi}{\partial t^2} + \frac{\partial\psi}{\partial z} = 0 \quad \text{on} \quad \Sigma_0, \tag{2.2c}$$

$$\psi(x,z,t+2\pi) \equiv \psi(x,z,t). \tag{2.2d}$$

Here Q_0 is the mean fluid volume, Σ_0 is the unperturbed free surface ($z = 0$), S refers to the mean wetted vertical walls of the stationary rectangle, S_B is the horizontal seabed, S_D is the bottom of the rectangular body, S_S is the artificial vertical wall caused by the Oz-symmetry and ν is the outer normal to the fluid boundary. The boundary condition (2.2*c*) results from combining the non-dimensional linearized kinematic and dynamic conditions

$$\frac{\partial\psi}{\partial z} = \frac{\partial f}{\partial t}, \qquad \Lambda\frac{\partial\psi}{\partial t} + f = 0 \quad \text{on} \quad \Sigma_0, \tag{2.3}$$

where $z = f(x,t)$ defines the free surface.

The two-dimensional free-boundary problem (2.2) requires a condition for $x \to -\infty$, which implies outgoing waves to the left, far from the body. In the case of steady-state 2π-periodic solutions, the most general representation of this condition is

$$\psi \sim F(\mathscr{K}x + t, z) \quad \text{as} \quad x \to -\infty, \tag{2.4}$$

where $\mathscr{K}$ is the wavenumber of the outgoing wave.

https://doi.org/10.1017/S002211200600440X Published online by Cambridge University Press

3. Solution method

3.1. *Reduction to integral equations*

3.1.1. *Domain decomposition, definitions*

In what follows, the linear problem (2.2) with (2.4) will be studied by using a domain-decomposition method. This suggests dividing Q_0 into four subdomains I, II, III and IV by auxiliary interfaces T_1, T_2 and T_3, as shown in figure 1(*b*), and setting appropriate transmission conditions on them. The division differs from an analogous procedure by Mavrakos (2004), who combined subdomains III and IV into one subdomain. Our reason for choosing separate subdomains III and IV is a requirement of nonlinear modal modelling (Faltinsen *et al.* 2000), which needs exact analytical fulfilment of the zero-Neumann condition on the hull walls for the linear solutions.

The method gives the motions inside the (II + III + IV)-domain as

$$\psi_{II+III+IV}(x,z,t)=\psi|_{(x,z)\in(II+III+IV)}=\varphi^{(1)}(x,z)\cos t+\varphi^{(2)}(x,z)\sin t. \tag{3.1}$$

This makes it possible to define the Neumann traces of $\varphi^{(i)}$, $i=1,2$, on T_j, $j=1,2,3$, as follows:

$$\text{on } T_1,\quad \frac{\partial\varphi^{(i)}}{\partial x}(-b,z)=w_1^{(i)}(z),\quad -h<z<-d, \tag{3.2a}$$

$$\text{on } T_2,\quad \frac{\partial\varphi^{(i)}}{\partial x}\left(-\tfrac{1}{2},z\right)=w_2^{(i)}(z),\quad -h<z<-d, \tag{3.2b}$$

$$\text{on } T_3,\quad \frac{\partial\varphi^{(i)}}{\partial z}(x,-d)=w_3^{(i)}(x),\quad -\tfrac{1}{2}<x<0. \tag{3.2c}$$

Here, the six functions $w_j^{(i)}$, $i=1,2$, $j=1,2,3$, belong to admissible functional spaces which provide the correctness of the corresponding boundary value problems. This reduces the original wave problem to a system of integral equations for the $w_j^{(i)}$, $i=1,2$, $j=1,2,3$.

3.1.2. *Solution in subdomain I*

In contrast with (3.1), to satisfy (2.4) the function $\psi_I(x,z,t)=\psi|_{(x,z)\in I}$ should include an outgoing-wave component. By separating spatial variables in the semi-infinite band and matching with solution (3.1) and the Neumann traces (3.2*a*), one obtains the following solution in I as a function of $w_1^{(1)}$ and $w_1^{(2)}$:

$$\begin{aligned}\psi_I(x,z,t)=&\int_{-h}^{-d}\left(w_1^{(1)}(z_0)\cos t+w_1^{(2)}(z_0)\sin t\right)\mathscr{G}_I(x,z;z_0)\,\mathrm{d}z_0\\&+\frac{\cosh(\mathscr{K}(z+h))}{\mathscr{K}N_0}\left[\sin(\mathscr{K}(x+b)+t)\int_{-h}^{-d}w_1^{(1)}(z_0)\cosh(\mathscr{K}(z_0+h))\,\mathrm{d}z_0\right.\\&\left.-\cos(\mathscr{K}(x+b)+t)\int_{-h}^{-d}w_1^{(2)}(z_0)\cosh(\mathscr{K}(z_0+h))\,\mathrm{d}z_0\right]\end{aligned} \tag{3.3}$$

where

$$\mathscr{G}_I(x,z;z_0)=\sum_{j=1}^{\infty}\frac{\cos\left(\kappa_j^{(1)}(z_0+h)\right)\cos\left(\kappa_j^{(1)}(z+h)\right)}{\kappa_j^{(1)}N_j^{(1)}}\exp\left(\kappa_j^{(1)}(x+b)\right). \tag{3.4}$$

In (3.3), $\mathscr{K}$ is the root of the transcendental equation

$$\mathscr{K}\tanh\mathscr{K}h=\Lambda,\quad \text{and}\quad N_0=\tfrac{1}{2}h(1+(\sinh 2\mathscr{K}h)/(2\mathscr{K}h)). \tag{3.5}$$

https://doi.org/10.1017/S002211200600440X Published online by Cambridge University Press

The $\{\kappa_i^{(1)}\}$ are the positive roots of

$$\kappa_i^{(1)} \tan \kappa_i^{(1)} h = -\Lambda, \qquad \text{and} \qquad N_i^{(1)} = \tfrac{1}{2}h\big(1 + \big(\sin 2\kappa_i^{(1)}h\big)\big/\big(2\kappa_i^{(1)}h\big)\big), \quad i \geqslant 1. \tag{3.6}$$

An analogous representation of the solution can be found, for instance, in Kuznetsov *et al.* (2001). Under certain mathematical circumstances, the integral formula (3.3) can be interpreted as a Green-function representation for the boundary-value problem in subdomain I (see Courant & Hilbert 1953, chapter 5, § 14) which expresses the solution in terms of the inhomogeneous Neumann traces at T_1. Analysing the structure of (3.4) shows that the first integral in (3.3) implies the vanishing of the evanescent-wave component as $x \to -\infty$, while the expression in the square brackets represents an outgoing wave.

3.1.3. *Solutions in subdomains II, III and IV*

The pairs $(w_1^{(i)}, w_2^{(i)})$, $i = 1, 2$, yeild part of the Neumann boundary-value problems for the Laplace equation in subdomain II. These problems have solutions (generally, to within unknown constants $\mathscr{A}_{-1}^{(i)}$) if and only if the following solvability conditions (see the appropriate theorems in Aubin 1972) are satisfied:

$$-\int_{-h}^{-d} w_1^{(i)}(z_0)\,\mathrm{d}z_0 + \int_{-h}^{-d} w_2^{(i)}(z_0)\,\mathrm{d}z_0 + \epsilon\delta_{2i}\underbrace{\int_{-b}^{-1/2} 1\,\mathrm{d}x_0}_{(b-1/2)} = 0, \quad i = 1, 2 \tag{3.7}$$

(δ_{ij} is the Kronecker delta). In a physical sense, (3.7) states instantaneous inflow–outflow balance through subdomain I. If (3.7) is true,

$$\varphi_{II}^{(i)}(x, z) = \mathscr{A}_{-1}^{(i)} + \epsilon\delta_{2i}\frac{(z+h)^2 - (x+b)^2}{2(h-d)} + \int_{-h}^{-d}\big[w_1^{(i)}(z_0)\,\mathscr{G}_{II}^{(1)}(x, z; z_0) + w_2^{(i)}(z_0)\,\mathscr{G}_{II}^{(2)}(x, z; z_0)\big]\,\mathrm{d}z_0, \quad i = 1, 2, \tag{3.8}$$

where

$$\mathscr{G}_{II}^{(1)}(x, z; z_0) = \frac{x}{h-d} - \sum_{j=1}^{\infty}\frac{\cos\big(\kappa_j^{(2)}(z_0+h)\big)\cos\big(\kappa_j^{(2)}(z+h)\big)}{\kappa_j^{(2)}N_j^{(2)}}\,\frac{\cosh\big(\kappa_j^{(2)}\big(x+\tfrac{1}{2}\big)\big)}{\cosh\big(\kappa_j^{(2)}\big(b-\tfrac{1}{2}\big)\big)}, \tag{3.9a}$$

$$\mathscr{G}_{II}^{(2)}(x, z; z_0) = \sum_{j=1}^{\infty}\frac{\cos\big(\kappa_j^{(2)}(z_0+h)\big)\cos\big(\kappa_j^{(2)}(z+h)\big)}{\kappa_j^{(2)}N_j^{(2)}}\,\frac{\cosh\big(\kappa_j^{(2)}(x+b)\big)}{\cosh\big(\kappa_j^{(2)}\big(b-\tfrac{1}{2}\big)\big)} \tag{3.9b}$$

with

$$\kappa_j^{(2)} = \frac{\pi j}{h-d}, \qquad N_j^{(2)} = \tfrac{1}{2}(h-d)\tanh\big(\kappa_j^{(2)}\big(b-\tfrac{1}{2}\big)\big), \quad j \geqslant 1. \tag{3.10}$$

Even though the solutions (3.8) are formally determined to within $\mathscr{A}_{-1}^{(i)}$, the actual values of these constants must be computed via the Dirichlet-transmission conditions on T_1, T_2 and T_3.

Analogously, $(w_2^{(i)}, w_3^{(i)})$, $i = 1, 2$, yield part of the Neumann boundary-value problem in subdomain III, which needs the solvability condition

$$\int_{-h}^{-d} w_2^{(i)}(z_0)\,\mathrm{d}z_0 - \int_{-1/2}^{0} w_3^{(i)}(x_0)\,\mathrm{d}x_0 = 0, \quad i = 1, 2. \tag{3.11}$$

https://doi.org/10.1017/S002211200600440X Published online by Cambridge University Press

Its solution is

$$\varphi^{(i)}_{III}(x,z) = \mathscr{A}^{(i)}_{-2} + \int_{-h}^{-d} w^{(i)}_2(z_0)\mathscr{G}^{(1)}_{III}(x,z;z_0)\,\mathrm{d}z_0 + \int_{-1/2}^{0} w^{(i)}_3(x_0)\mathscr{G}^{(2)}_{III}(x,z;x_0)\,\mathrm{d}x_0, \quad i=1,2, \tag{3.12}$$

where the $\mathscr{A}^{(i)}_{-2}$ are also computed from the Dirichlet transmission conditions and

$$\mathscr{G}^{(1)}_{III}(x,z;z_0) = -\frac{x^2-(z+h)^2}{h-d} - \sum_{j=1}^{\infty} \frac{\cos\left(\kappa^{(2)}_j(z_0+h)\right)\cos\left(\kappa^{(2)}_j(z+h)\right)}{\kappa^{(2)}_j N^{(3)}_j} \frac{\cosh\left(\kappa^{(2)}_j x\right)}{\cosh\left(\frac{1}{2}\kappa^{(2)}_j\right)}, \tag{3.13a}$$

$$\mathscr{G}^{(2)}_{III}(x,z;x_0) = \sum_{j=1}^{\infty} \frac{\cos\left(\kappa^{(3)}_j x_0\right)\cos\left(\kappa^{(3)}_j x\right)}{\kappa^{(3)}_j N^{(4)}_j} \cdot \frac{\cosh\left(\kappa^{(3)}_j(z+d)\right)}{\cosh\left(\kappa^{(3)}_j(h-d)\right)} \tag{3.13b}$$

with

$$\kappa^{(3)}_j = 2\pi j, \qquad N^{(3)}_j = \tfrac{1}{2}(h-d)\tanh\left(\tfrac{1}{2}\kappa^{(2)}_j\right), \qquad N^{(4)}_j = \tfrac{1}{4}\tanh\left(\kappa^{(3)}_j(h-d)\right), \quad j \geqslant 1. \tag{3.14}$$

Finally, the mixed boundary-value problems in subdomain IV involving the Neumann boundary condition (3.2*c*) have a unique solution if and only if the analogous homogeneous problems have only trivial solutions. This occurs when

$$\Lambda \neq \kappa^{(3)}_j \tanh\left(\kappa^{(3)}_j d\right), \quad j \geqslant 1. \tag{3.15}$$

In contrast with (3.7) and (3.11), the solvability condition (3.15) has no physical interpretation but is easily yielded by our method. However, (3.15) has physical meaning when subdomain IV represents a closed tank and we consider the forced motion of this tank. Equation (3.15) states then that a solution is not possible at the natural sloshing frequencies. However, as will be discussed below, the singularity due to (3.15) is removable for the entire problem.

The mixed boundary-value problems in subdomain IV have the following solution:

$$\varphi^{(i)}_{IV}(x,z) = \int_{-1/2}^{0} w^{(i)}_3(x_0)\mathscr{G}_{IV}(x,z;x_0)\,\mathrm{d}x_0, \quad i=1,2, \tag{3.16}$$

where

$$\mathscr{G}_{IV}(x,y;x_0) = 2\left(z+\frac{1}{\Lambda}\right) + \sum_{j=1}^{\infty} \frac{\cos\left(\kappa^{(3)}_j x_0\right)\cos\left(\kappa^{(3)}_j x\right)}{\kappa^{(3)}_j N^{(5)}_j} \frac{\kappa^{(3)}_j\cosh\left(\kappa^{(3)}_j z\right)+\Lambda\sinh\left(\kappa^{(3)}_j z\right)}{\kappa^{(3)}_j\cosh\left(\kappa^{(3)}_j d\right)} \tag{3.17}$$

and

$$N^{(5)}_j = \frac{1}{4}\left[\frac{\Lambda}{\kappa^{(3)}_j} - \tanh\left(\kappa^{(3)}_j d\right)\right]. \tag{3.18}$$

The kernel (3.17) becomes unbounded as Λ tends to the critical values defined by (3.15) because this limit causes $N^{(5)}_j \to 0$ for a certain j.

https://doi.org/10.1017/S002211200600440X Published online by Cambridge University Press

In the same way as for (3.3), the integral formulae (3.8), (3.12) and (3.16) may be interpreted as a Green-function representation for the corresponding free-boundary problems in subdomains II–IV, i.e. an 'inversion' of these problems defined in an operator form. The series-based integral kernels $\mathscr{G}_i^{(k)}$, $i = I, \ldots, IV$, are common in the literature on the domain-decomposition method (see Drobyshevski 2004; Kuznetsov *et al.* 2001; Mavrakos 2004; Porter & Evans 1995; Williams & Abul-Azm 1997). An alternative is to express solutions in the subdomains by means of Green's identity, with a velocity potential and a log-type Green function for each subdomain. The latter technique is typical of boundary-element methods in marine hydrodynamics. However, the log-type representation is rarely used in the domain-decomposition method because, in its general form, the representation couples both the Neumann and the Dirichlet traces on the transmission lines. As a consequence, (3.3), (3.8), (3.12) and (3.16) may contain additional quantities relating to projections of the velocity potential on T_i and other boundaries. This makes it difficult to derive the governing integral equations on the transmission lines, as discussed later in the text. Special efforts should be made to avoid Dirichlet traces. For instance, their use implies that the log-type Green function in subdomains II and III must satisfy the zero-Neumann condition on their boundaries. We did not try to find the corresponding expressions. The main reason was that our special singular functional basis in the Galerkin scheme, to be discussed below, admits exact integrals in all the computations, while we do not know of analogous exact integrals over the corresponding expressions for log-type kernels.

3.1.4. *Dirichlet transmission and the resulting integral equations*

The problem is reduced to a set of integral equations with respect to $w_j^{(i)}$, $j = 1, 2, 3$, $i = 1, 2$, by using the Dirichlet transmission conditions on T_j, which imply that

$$\psi_I(-b, z, t) = \varphi_{II}^{(1)}(-b, z)\cos t + \varphi_{II}^{(2)}(-b, z)\sin t, \quad -h < z < -d, \quad t \geqslant 0 \tag{3.19}$$

as well as

$$\begin{aligned} &\varphi_{II}^{(i)}\left(-\tfrac{1}{2}, z\right) = \varphi_{III}^{(i)}\left(-\tfrac{1}{2}, z\right), \quad -h < z - d, \\ &\varphi_{III}^{(i)}(x, -d) = \varphi_{IV}^{(i)}(x, -d), \quad -\tfrac{1}{2} < x < 0, \quad i = 1, 2. \end{aligned} \tag{3.20}$$

Together with the solvability conditions (3.7) and (3.11), (3.19) and (3.20) yield the following system of integral equations:

$$\left.\begin{aligned} &\int_{-h}^{-d} w_1^{(1)}(z_0)\mathscr{K}_{1,1}(z, z_0)\,\mathrm{d}z_0 + \int_{-h}^{-d} w_2^{(1)}(z_0)\mathscr{K}_{1,2}(z, z_0)\,\mathrm{d}z_0 - \mathscr{A}_{-1}^{(1)} \\ &\quad - \frac{\cosh(\mathscr{K}(z+h))}{\mathscr{K}N_0}\int_{-h}^{-d} w_1^{(2)}(z_0)\cosh(\mathscr{K}(z_0+d))\,\mathrm{d}z_0 = 0, \\ &\int_{-h}^{-d} w_1^{(2)}(z_0)\mathscr{K}_{1,1}(z, z_0)\,\mathrm{d}z_0 + \int_{-h}^{-d} w_2^{(2)}(z_0)\mathscr{K}_{1,2}(z, z_0)\,\mathrm{d}z_0 - \mathscr{A}_{-1}^{(2)} \\ &\quad + \frac{\cosh(\mathscr{K}(z+h))}{\mathscr{K}N_0}\int_{-h}^{-d} w_1^{(1)}(z_0)\cosh(\mathscr{K}(z_0+h))\,\mathrm{d}z_0 = \epsilon\frac{(z+h)^2}{2(h-d)}, \\ &\qquad\qquad -h < z < -d, \end{aligned}\right\} \tag{3.21a}$$

$$\int_{-h}^{-d} w_1^{(i)}(z_0)\mathscr{K}_{2,1}(z, z_0)\,\mathrm{d}z_0 + \int_{-h}^{-d} w_2^{(i)}(z_0)\mathscr{K}_{2,2}(z, z_0)\,\mathrm{d}z_0 + \int_{-1/2}^{0} w_3^{(i)}(x_0)\mathscr{K}_{2,3}(z, x_0)\,\mathrm{d}x_0$$
$$+ \mathscr{A}_{-1}^{(i)} - \mathscr{A}_{-2}^{(i)} = -\epsilon\delta_{2i}\frac{(z+h)^2 - \left(b - \frac{1}{2}\right)^2}{2(h-d)}, \quad -d < z < -h, \tag{3.21b}$$

https://doi.org/10.1017/S002211200600440X Published online by Cambridge University Press

$$\int_{-h}^{-d} w_2^{(i)}(z_0)\mathscr{K}_{3,2}(x,z_0)\,\mathrm{d}z_0 + \int_{-1/2}^{0} w_3^{(i)}(x_0)\mathscr{K}_{3,3}(x,x_0)\,\mathrm{d}x_0 + \mathscr{A}_{-2}^{(i)} = 0, \quad -\tfrac{1}{2} < x < 0, \tag{3.21c}$$

$$\int_{-h}^{-d} w_1^{(i)}(z_0)\,\mathrm{d}z_0 - \int_{-h}^{-d} w_2^{(i)}(z_0)\,\mathrm{d}z_0 = \epsilon\delta_{2i}\left(b-\tfrac{1}{2}\right), \tag{3.21d}$$

$$\int_{-h}^{-d} w_2^{(i)}(z_0)\,\mathrm{d}z_0 - \int_{-1/2}^{0} w_3^{(i)}(x_0)\,\mathrm{d}x_0 = 0, \tag{3.21e}$$

for $i = 1, 2$. The kernels are defined as follows:

$$\begin{aligned}\mathscr{K}_{1,1}(z,z_0) &= \mathscr{G}_I(-b,z;z_0) - \mathscr{G}_{II}^{(1)}(-b,z;z_0)\\ &= \frac{b}{h-d} + \sum_{j=1}^{\infty}\frac{\cos\left(\kappa_j^{(1)}(z_0+h)\right)\cos\left(\kappa_j^{(1)}(z+h)\right)}{\kappa_j^{(1)}N_j^{(1)}}\\ &\quad + \sum_{j=1}^{\infty}\frac{\cos\left(\kappa_j^{(2)}(z_0+h)\right)\cos\left(\kappa_j^{(2)}(z+h)\right)}{\kappa_j^{(2)}N_j^{(2)}},\end{aligned} \tag{3.22a}$$

$$\mathscr{K}_{1,2}(z,z_0) = -\mathscr{G}_{II}^{(2)}(-b,z;z_0) = -\sum_{j=1}^{\infty}\frac{\cos\left(\kappa_j^{(2)}(z_0+h)\right)\cos\left(\kappa_j^{(2)}(z+h)\right)}{\kappa_j^{(2)}N_j^{(2)}\cosh\left(\kappa_j^{(2)}\left(b-\frac{1}{2}\right)\right)}, \tag{3.22b}$$

$$\begin{aligned}\mathscr{K}_{2,1}(z,z_0) &= \mathscr{G}_{II}^{(1)}\left(-\tfrac{1}{2},z;z_0\right)\\ &= -\frac{1}{2(h-d)} - \sum_{j=1}^{\infty}\frac{\cos\left(\kappa_j^{(2)}(z_0+h)\right)\cos\left(\kappa_j^{(2)}(z+h)\right)}{\kappa_j^{(2)}N_j^{(2)}\cosh\left(\kappa_j^{(2)}\left(b-\frac{1}{2}\right)\right)},\end{aligned} \tag{3.22c}$$

$$\begin{aligned}\mathscr{K}_{2,2}(z,z_0) &= \mathscr{G}_{II}^{(2)}\left(-\tfrac{1}{2},z;z_0\right) - \mathscr{G}_{III}^{(1)}\left(-\tfrac{1}{2},z;z_0\right)\\ &= -\frac{(z+h)^2}{h-d} + \frac{1}{4(h-d)} + \sum_{j=1}^{\infty}\frac{\cos\left(\kappa_j^{(2)}(z_0+h)\right)\cos\left(\kappa_j^{(2)}(z+h)\right)}{\kappa_j^{(2)}}\\ &\quad\times\left(\frac{1}{N_j^{(2)}} + \frac{1}{N_j^{(3)}}\right),\end{aligned} \tag{3.22d}$$

$$\mathscr{K}_{2,3}(z,x_0) = -\mathscr{G}_{III}^{(2)}\left(-\tfrac{1}{2},z;x_0\right) = -\sum_{j=1}^{\infty}(-1)^j\frac{\cos\left(\kappa_j^{(3)}x_0\right)}{\kappa_j^{(3)}N_j^{(4)}}\frac{\cosh\left(\kappa_j^{(3)}(z+h)\right)}{\cosh\left(\kappa_j^{(3)}(h-d)\right)}, \tag{3.22e}$$

$$\begin{aligned}\mathscr{K}_{3,2}(x,z_0) &= \mathscr{G}_{III}^{(1)}(x,-d;z_0)\\ &= h-d-\frac{x^2}{h-d} - \sum_{j=1}^{\infty}(-1)^j\frac{\cos\left(\kappa_j^{(2)}(z_0+h)\right)}{\kappa_j^{(2)}N_j^{(3)}}\frac{\cosh\left(\kappa_j^{(2)}x\right)}{\cosh\left(\frac{1}{2}\kappa_j^{(2)}\right)},\end{aligned} \tag{3.22f}$$

$$\begin{aligned}\mathscr{K}_{3,3}(x,x_0) &= \mathscr{G}_{III}^{(2)}(x,-d;x_0) - \mathscr{G}_{IV}(x,-d;x_0)\\ &= 2\left(d-\frac{1}{\Lambda}\right) + \sum_{j=1}^{\infty}\frac{\cos\left(\kappa_j^{(3)}x_0\right)\cos\left(\kappa_j^{(3)}x\right)}{\kappa_j^{(3)}N_j^{(6)}},\end{aligned} \tag{3.22g}$$

where

$$\frac{1}{N_j^{(6)}} = 4\left(\coth\left(\kappa_j^{(3)}(h-d)\right) - \frac{\kappa_j^{(3)} - \Lambda\tanh\left(\kappa_j^{(3)}d\right)}{\Lambda - \kappa_j^{(3)}\tanh\left(\kappa_j^{(3)}d\right)}\right).$$

https://doi.org/10.1017/S002211200600440X Published online by Cambridge University Press

One should note that, if Λ tends to its critical value defined by (3.15) at a fixed j, the kernel $\mathscr{K}_{3,3}$ becomes formally singular (infinite) owing to division by zero in a single summand of the sum. However, the singularity is removable for the complete integral problem: multiplying (3.21*c*) by $\Lambda - \kappa_j^{(3)} \tanh(\kappa_j^{(3)} d)$ and performing simple algebraic operations make the integral equation (3.21*c*) well-posed. This means that the formal solvability condition (3.15) is unnecessary for the complete system of integral equations (3.21).

3.2. *Galerkin method*

3.2.1. *Projective scheme*

The inhomogeneous system of ten integral equations (3.21) couples six unknown functions $w_k^{(i)}$, $k = 1, 2, 3$, $i = 1, 2$, and four coefficients $\mathscr{A}_{-1}^{(i)}, \mathscr{A}_{-2}^{(i)}$, $i = 1, 2$. It can be solved by the Galerkin projective scheme, suggesting approximate solutions in the form

$$w_1^{(i)}(z) = \sum_{j=1}^{N_1} \alpha_j^{(1,i)} v_j^{(1)}(z), \quad w_2^{(i)}(z) = \sum_{j=1}^{N_2} \alpha_j^{(2,i)} v_j^{(1)}(z), \quad w_3^{(i)}(x) = \sum_{j=1}^{N_3} \alpha_j^{(3,i)} v_j^{(2)}(x), \quad (3.23)$$

where $\{v_j^{(1)}\}$ and $\{v_j^{(2)}\}$ are two complete systems of functions on $(-h, -d)$ and $(-\frac{1}{2}, 0)$, respectively. Insertion of (3.23) into (3.21) and use of the projective scheme leads to a system of $2N_1 + 2N_2 + 2N_3 + 4$ linear equations with respect to $2N_1 + 2N_3 + 2N_3 + 4$ variables, $\{\alpha_j^{(1,i)}, j = 1, \ldots, N_1\}$, $\{\alpha_j^{(2,i)}, j = 1, \ldots, N_2\}$, $\{\alpha_j^{(3,i)}, j = 1, \ldots, N_3\}$ and $\mathscr{A}_{-j}^{(i)}$, $i, j = 1, 2$.

By introducing the vector

$$\begin{aligned} \boldsymbol{B} = \big(&\alpha_1^{(1,1)} \cdots \alpha_{N_1}^{(1,1)} \alpha_1^{(2,1)} \cdots \alpha_{N_2}^{(2,1)} \alpha_1^{(3,1)} \cdots \alpha_{N_3}^{(3,1)} \mathscr{A}_{-2}^{(1)} \mathscr{A}_{-1}^{(1)} \\ &\alpha_1^{(1,2)} \cdots \alpha_{N_1}^{(1,2)} \alpha_1^{(2,2)} \cdots \alpha_{N_2}^{(2,2)} \alpha_1^{(3,2)} \cdots \alpha_{N_3}^{(3,2)} \mathscr{A}_{-2}^{(2)} \mathscr{A}_{-1}^{(2)}\big)^T, \end{aligned} \quad (3.24)$$

the matrix problem following from the Galerkin scheme is as follows:

$$\boldsymbol{P}\boldsymbol{B} = \epsilon \boldsymbol{b}, \quad (3.25)$$

where $\boldsymbol{P}$ is a $(2N_1 + 2N_3 + 2N_3 + 4) \times (2N_1 + 2N_3 + 2N_3 + 4)$ matrix.

The elements of $\boldsymbol{P}$ and the right-hand-side vector $\boldsymbol{b}$ are integrals over the kernels (3.22) and the functions $\{v_j^{(1)}\}$ and $\{v_j^{(2)}\}$. The matrix $\boldsymbol{P}$ has the following structure:

$$\boldsymbol{P} = \left(\begin{array}{c|c} \boldsymbol{D} & -\boldsymbol{p} \\ & 0 \\ \hline \boldsymbol{p} & \boldsymbol{D} \\ 0 & \end{array}\right), \quad (3.26)$$

where the two sub-matrices $\boldsymbol{D}$ and $\boldsymbol{p}$ have dimensions $(N_1 + N_2 + N_3 + 2) \times (N_1 + N_2 + N_3 + 2)$ and $N_1 \times N_1$, respectively.

3.2.2. *Local velocity field at the corner points $\bar{A}_2$ and $\bar{A}_3$ and a functional basis*

The convergence and accuracy of the Galerkin method depend on how the functional sets $\{v_j^{(1)}(z)\}$ and $\{v_j^{(2)}(x)\}$ are chosen. Because the Neumann traces on T_k, $k = 1, 2, 3$, are singular at the corner points of the piercing rectangular body, i.e. $w_j^{(i)}(z) \to \infty$ as $z \to -d$ and $w_3^{(i)}(x) \to \infty$ as $x \to -\frac{1}{2}$, the use of a smooth functional basis, for instance, a trigonometrical or polynomial basis, causes weak convergence. In contrast, accounting for the singular character of the traces should improve the convergence (Porter & Evans 1995; Kuznetsov *et al.* 2001; Gavrilyuk *et al.* 2006). The

https://doi.org/10.1017/S002211200600440X Published online by Cambridge University Press

local solutions of the complex velocity at the edges $\bar{A}_2$ and $\bar{A}_3$ can be expressed in the complex plane $Z=\bar{x}+\mathrm{i}\bar{z}$ as

$$\left.\frac{\mathrm{d}W_0}{\mathrm{d}Z}\right|_{\mathrm{at}\,\bar{A}_2} = \mathrm{e}^{-\mathrm{i}\pi/2}\,\eta_{3a}\sigma\sin\sigma t + \sum_{i=1}^{\infty} T_i^{(2)}(t)(Z+\bar{B}+\mathrm{i}\bar{d})^{2i/3-1}, \tag{3.27a}$$

$$\left.\frac{\mathrm{d}W_0}{\mathrm{d}Z}\right|_{\mathrm{at}\,\bar{A}_3} = \mathrm{e}^{-\mathrm{i}\pi/2}\,\eta_{3a}\sigma\sin\sigma t + \sum_{i=1}^{\infty} T_i^{(3)}(t)\left[\mathrm{e}^{\mathrm{i}\pi}\left(Z+\frac{L_1}{2}+\mathrm{i}\bar{d}\right)\right]^{2i/3-1}, \tag{3.27b}$$

where W_0 is the complex velocity potential. The first terms in (3.27a, b) are caused by the vertical motion of the body. Conclusions on the asymptotic behaviour of the velocity potential ψ at the corner points may also be found in the book by Grisvard (1985).

By conducting direct analytical derivations, or by noting that summands in (3.27) for which i is divisible by 3 are regular, one can see that terms associated with $T_{3l}^{(2)}(t)$, $T_{3l}^{(3)}(t)$, $l=1,2,\ldots$ vanish on the intervals $\bar{T}_k$, $k=1,2,3$. This implies that $\psi(-b,z,t)\sim(z+d)^m$ as $z\to-d$ and that $\psi(x,-d,t)\sim(x+\frac{1}{2})^m$ as $x\to-\frac{1}{2}$, where the numbers m belong to the set

$$\left\{\pm\frac{1}{3}+2(i-1),\ i\geqslant 1\right\}. \tag{3.28}$$

The enumeration of (3.28) in ascending order determines a sequence m_j, $j\geqslant 1$. The functional basis must satisfy

$$v_j^{(1)}\sim(z+d)^{m_j},\quad z\to-d;\qquad v_j^{(2)}\sim\left(x+\tfrac{1}{2}\right)^{m_j},\quad x\to-\tfrac{1}{2}\qquad j\geqslant 1. \tag{3.29}$$

Further, accounting for the zero-Neumann conditions on S_B and S_S, i.e.

$$\left(v_j^{(1)}\right)'(-h)=0\quad\text{and}\quad\left(v_j^{(2)}\right)'(0)=0,\quad j\geqslant 1, \tag{3.30}$$

we may deduce from (3.29) the following functional sets:

$$v_j^{(1)}(z)=\frac{1}{r_j^{(1)}}\left(1-\left(\frac{z+h}{h-d}\right)^2\right)^{m_j},\quad v_j^{(2)}(x)=\frac{1}{r_j^{(2)}}(1-(2x)^2)^{m_j},\quad j\geqslant 1, \tag{3.31}$$

where

$$r_j^{(1)}=\sqrt{\frac{(h-d)\sqrt{\pi}\Gamma(2m_j+1)}{2\Gamma\left(2m_j+\frac{3}{2}\right)}},\quad r_j^{(2)}=\frac{1}{2}\sqrt{\frac{\sqrt{\pi}\Gamma(2m_j+1)}{\Gamma\left(2m_j+\frac{3}{2}\right)}},\quad j\geqslant 1. \tag{3.32}$$

Here $\Gamma(\cdot)$ is the gamma function. The scaling factors $r_j^{(i)}$, $i=1,2$, $j=1,2,3$, appear from the normalization condition $\int_{-h}^{-d}(v_j^{(1)}(z))^2\,\mathrm{d}z=\int_{-1/2}^{0}(v_j^{(2)}(x))^2\,\mathrm{d}x=1$, $j\geqslant 1$.

The non-singular subsets $\{v_j^{(1)}\}$ and $\{v_j^{(2)}\}$ with $j\geqslant 2$ constitute complete bases for the functions on the intervals $[-h,-d]$ and $[-\frac{1}{2},0]$, respectively, for functions which satisfy (3.30). The completeness follows from the classical theorem of Müntz† (see Müntz 1914; Erdélyi & Johnson 2001). Because $v_1^{(1)}$ and $v_1^{(2)}$ belong to square integrable functions, the full sets (3.31) are complete in the mean-square metrics.

† Theorem *Let $p\in(0,\infty)$. Suppose that $(\lambda_j)_{j=0}^{\infty}$ is a sequence with $0\leqslant\lambda_0<\lambda_1<\lambda_2<\cdots$. The span $\{x^{\lambda_0},x^{\lambda_1},\ldots\}$ is dense in $L_p[0,1]$ if and only if $\sum_{j=1}^{\infty}1/\lambda_j=\infty$.*
In our case, $\lambda_i=m_i$ and the condition $\sum_{j=1}^{\infty}1/m_j=\infty$ is fulfilled.

https://doi.org/10.1017/S002211200600440X Published online by Cambridge University Press

Moreover, $v_1^{(1)}$ and $v_1^{(2)}$ may be associated with approximations of the singular velocity component, while the complete functional bases $\{v_j^{(1)}\}$ and $\{v_j^{(2)}\}$ $j \geqslant 2$ approximate its regular component.

Comparing the polynomial terms in (3.27) with asymptotic properties of the base functions (3.31) shows that $T_i^{(2)}(t)$ and $T_i^{(3)}(t)$, $i \neq 3l$, in (3.27) are uniquely determined by the corresponding Galerkin coefficients $\alpha_k^{(i,j)}$. In particular, we can write the singular dimensional horizontal-velocity component at $\bar{A}_k$, $k = 2, 3$, as

$$\left.\frac{\partial \bar{\psi}}{\partial \bar{x}}\right|_{\bar{x}=-\bar{b}} \approx L_1^{4/3}\sigma(-\bar{d}-\bar{z})^{-1/3}\gamma\left(\alpha_1^{(1,1)}\cos\sigma t + \alpha_1^{(1,2)}\sin\sigma t\right)$$
$$= L_1^{4/3}\sigma(-\bar{d}-\bar{z})^{-1/3}\gamma\sqrt{\left(\alpha_1^{(1,1)}\right)^2+\left(\alpha_1^{(1,2)}\right)^2}\ \sin(\sigma t+\theta_{A_2}), \quad (3.33a)$$

$$\left.\frac{\partial \bar{\psi}}{\partial \bar{x}}\right|_{\bar{x}=-L_1/2} \approx L_1^{4/3}\sigma(-\bar{d}-\bar{z})^{-1/3}\gamma\left(\alpha_1^{(2,1)}\cos\sigma t + \alpha_1^{(2,2)}\sin\sigma t\right)$$
$$= L_1^{4/3}\sigma(-\bar{d}-\bar{z})^{-1/3}\gamma\sqrt{\left(\alpha_1^{(2,1)}\right)^2+\left(\alpha_1^{(2,2)}\right)^2}\ \sin(\sigma t+\theta_{A_3}) \quad (3.33b)$$

as $\bar{z} \to -\bar{d}-0$, where

$$\gamma = \frac{1}{r_1^{(1)}}\left(\frac{h-d}{2}\right)^{1/3} = 0.487\,570\,209\,581\,027\cdots\left(\frac{h-d}{2}\right)^{-1/6}, \quad (3.34)$$

$$\cos\theta_{A_k} = \frac{\alpha_1^{(k-1,2)}}{\sqrt{\left(\alpha_1^{(k-1,1)}\right)^2+\left(\alpha_1^{(k-1,2)}\right)^2}},\ \sin\theta_{A_k} = \frac{\alpha_1^{(k-1,1)}}{\sqrt{\left(\alpha_1^{(k-1,1)}\right)^2+\left(\alpha_1^{(k-1,2)}\right)^2}}, \quad (3.35)$$

for $k = 2, 3$.

Comparison with (3.27) gives

$$T_1^{(k)}(t) = L_1^{4/3}\sigma\frac{2\gamma}{\sqrt{3}}\sqrt{\left(\alpha_1^{(k-1,1)}\right)^2+\left(\alpha_1^{(k-1,2)}\right)^2}\sin(\sigma t+\theta_{A_k}), \quad k=2,3. \quad (3.36)$$

3.3. *Trapping and resonance condition*

Physically, the non-existence of a solution of the radiation problem (2.2) (and, as a result, of the system of integral equations (3.21)) for a certain Λ_* could be associated with the existence of a trapped mode. Although the rectangular geometry most probably does not admit such a trapping, the authors were not able to find suitable theorems. However, there exists a necessary condition $\sin 2\mathscr{K} > 0$ from the book by Kuznetsov *et al.* (2002) (see the proposition on p. 175), which makes it possible to estimate the admissible ranges of Λ_*, where Oz-symmetric trapping may be possible. This condition predicts the range of the lowest resonance frequency causing piston-like motion to be $\Lambda_* \in (0, (\pi/2)\tanh(\pi/2))$.

Furthermore, the concept of trapped (or nearly trapped) modes is very useful for evaluating the resonant frequencies $\Lambda_* \in (0, (\pi/2)\tanh(\pi/2))$ at which a maximum piston-like amplitude is expected. Indeed, the trapping implies a non-trivial solution of the corresponding homogeneous problem ($\epsilon = 0$), which has a zero outgoing wave component. This leads to two necessary conditions to be satisfied simultaneously. The first condition is

$$\int_{-h}^{-d} w_1^{(i)}(z_0)\cosh(\mathscr{K}(z_0+h))\,\mathrm{d}z_0 = 0, \quad i = 1, 2, \quad (3.37)$$

https://doi.org/10.1017/S002211200600440X Published online by Cambridge University Press

i.e. that the square-bracketed terms in (3.3) vanish (the zero-outgoing-wave condition). By examining the structure of the integral equation (3.21*a*), the integral condition (3.37) is seen to be equivalent to

$$\boldsymbol{p}\ \left(\alpha_1^{(1,i)}\ \cdots\ \alpha_{N_1}^{(1,i)}\right)^T = \mathbf{0}, \quad i = 1, 2 \tag{3.38}$$

($\boldsymbol{p}$ is the $N_1 \times N_1$ submatrix in (3.26)) for an approximate trapped-mode solution. This means that the two asymmetric blocks in $\boldsymbol{P}$ associated with $\boldsymbol{p}$ are responsible for the outgoing wave component. Further, if (3.38) is fulfilled, owing to the symmetry of the matrix $\boldsymbol{P}$, the non-trivial solution must satisfy the second necessary condition,

$$\det \|\boldsymbol{D}(\Lambda_*)\| = 0, \qquad \Lambda_* \in \left(0, \frac{\pi}{2}\tanh\frac{\pi}{2}\right), \tag{3.39}$$

where $\boldsymbol{D}$ is the submatrix of dimension $N_1 + N_2 + N_3 + 2$ found in (3.26).

Considering (3.38) and (3.39) together shows that the second condition makes it possible to compute the Λ_* value at which a piston-like trapped mode is possible. Let us focus on the limit $\Lambda \to \Lambda_*$ and assume that (3.38) is not fulfilled at $\Lambda = \Lambda_*$ but that the corresponding outgoing wave terms (3.21*a*) are small relative to the norm of the evanescent component. The latter means that the left-hand side of (3.38) is not zero but small relative to ϵ as $\Lambda \to \Lambda_*$. Under this condition, i.e. asymptotically in terms of the smallness of (3.38), the condition (3.39) means that the evanescent component becomes infinite in the scale ϵ as $\Lambda \to \Lambda_*$. Therefore, throughout this paper, the roots of (3.39) in the limit $N_1, N_2, N_3 \to \infty$ are called the resonant frequencies. At these frequencies, the maximum wave elevation in the moonpool of the evanescent component is expected. Because our definition of the resonant frequency is argued with specific asymptotic assumptions and, generally speaking, there is no rigorous mathematical proof of the fact that Λ_* leads to the maximum amplitude of the evanescent component, a broad spectrum of calculations was done. Unless the dimensionless quantities B and d tend to 0 for a fixed finite h, our numerical experiments have established that there is one and only one root of (3.39) and confirmed that the maximum amplitude of the piston-like mode occurs at $\Lambda = \Lambda_*$.

Further, after identifying the resonant frequencies Λ_* and computing an appropriate non-trivial solution $\boldsymbol{B}_1$ from $\boldsymbol{D}(\Lambda_*)\boldsymbol{B}_1 = \mathbf{0}$ we verified numerically the non-existence of a trapped piston-like mode. (Because a trapped mode oscillates freely, without loss of generality the trapped-mode solution can be chosen for convenience as having zero phase: $\boldsymbol{B} = (\boldsymbol{B}_1, \mathbf{0})$.) With this aim in mind, we calculated the ratio of the outgoing-wave amplitude and the piston-wave amplitude associated with $\boldsymbol{B} = (\boldsymbol{B}_1, \mathbf{0})$ from (4.2) and (4.5) below. By evaluating the ratio as a function of the geometric parameters, we conducted extensive computations to identify its zeroes (i.e. small values). These showed that the ratio is finite, positive and much larger than the maximum numerical error, estimated as 10^{-6}, at least for the geometric shapes related to our model test cases.

3.4. *Convergence and numerical details*

The functional basis (3.31) makes it possible to get analytical expressions for the elements of $\boldsymbol{P}$ and $\boldsymbol{b}$ in terms of the gamma and Bessel functions. Quadrature formulae are not needed.† Analysis of these expressions identifies the numerical summation of

† These explicit expressions are given in a supplement available with the online version of the paper.

https://doi.org/10.1017/S002211200600440X Published online by Cambridge University Press

truncated series by Bessel functions as the most CPU-expensive operation (a similar situation appeared in the papers of Porter & Evans (1995), Kuznetsov *et al.* (2001), Gavrilyuk *et al.* (2006), where the functional basis captured the singularities at the sharp edges of baffles and barriers). These summations are CPU-demanding even in the case when, as organized in our code, the Bessel-function calculation switches to an asymptotic formula with increasing summation index j. After fixing the number of desired significant figures for the above-mentioned sums, the truncation number becomes a function of the indexes i and k. The weakest convergence is expected only for the six different series associated with $i=k=1$ (because $\kappa_j^{(1)} \sim j,\ \ j \to \infty$; see the online supplementary). These series need, for instance, one million terms to guarantee eight significant figures in the sum. (All the numerical results were made to guarantee these eight significant figures after truncations.) Other summations are not CPU-demanding. For example, even $i=1,\ k=2$ requires only about 10 000 terms but, when $i+k>3$, the numerical summation needs less than 2500–50 terms to get the same eight significant figures. We should stress that only a limited set of terms change with Λ. By storing the remaining terms, the study of approximate solutions as a function of Λ becomes less CPU-demanding. For example, for a single frequency Λ with $N_1=N_2=N_3=8$ and eight significant figures for the sums the calculation needs less than 2 seconds for our non-optimized FORTRAN code on a Pentium-IV (2.6 GHz) computer.

The method guarantees six to seven significant figures with $q=N_1=N_2=N_3=7-8$ for the tested values of h, B and d. This is consistent with the above-mentioned summations providing eight significant figures. The same convergence was observed for various other finite h, b and d values. The convergence is very fast for smaller $h-d$ values, corresponding to a narrow gap between the seabed and the hulls, and weaker for fairly deep water. The latter is caused by the obvious fact that the functional basis (3.31) does not decay exponentially downwards as it does the infinite in deep-water wave problem.

Convergence of the Galerkin-method results to the solution of the original integral equations depends on the properties of $\boldsymbol{P}$ in (3.25). The tested configurations (d, B, h) lead to non-zero (strongly positive) determinants of $\boldsymbol{P}$. However, this determinant demonstrated a minimum at $\Lambda=\Lambda_*$, where Λ_* is the resonant frequency associated with the root of (3.39). This explains why the convergence may generally differ as Λ varies, especially as $\Lambda \to \Lambda_*$. Typical convergence is demonstrated in the tables of the online supplement. The method provides from six to seven significant figures for the amplitude parameters $\mathscr{A}_j^{(i)},\ \ j=0,1,\ \ i=1,2$, defined by (4.2) and (4.5) below (scaled by the forcing amplitude; see the approximate formulae in the online supplement) for both resonant and non-resonant conditions. The theoretical results were controlled by the volume- and energy-conservation conditions and asymptotic solutions as $\Lambda \to 0$ were derived. This is discussed below in § 4.2.3.

The accuracy of the method can be improved by using larger truncated series in the corresponding approximate formulae and performing a Gram–Schmidt orthogonalization of the functional basis (3.31). The latter may be necessary for large $N_i, i=1,2,3$, because of the non-orthogonality of (3.31) in the mean-square metrics. As a consequence, the determinant of the corresponding large-dimensional Gram matrix over the functional sets (3.31) tends to zero and, therefore, $\det|D|$ and $\det|\boldsymbol{P}|$ become numerically smaller than the chosen precision for certain $q \geqslant q_*$. Improving the summation and performing the orthogonalization significantly increases the required CPU time so that, for example, providing nine to ten significant figures (i.e. an additional two significant digits) increases the CPU time by a factor 1000.

https://doi.org/10.1017/S002211200600440X Published online by Cambridge University Press

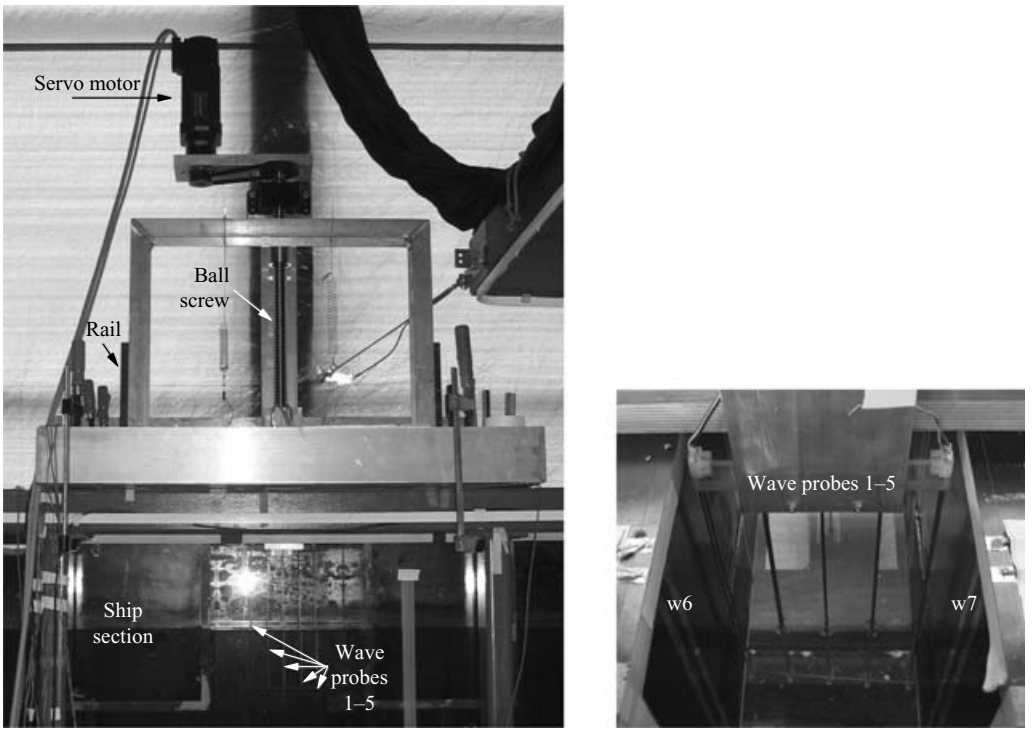


FIGURE 2. Picture of the test rig and details of the wave probes w1–w7.

However, to maintain computational efficiency we found it satisfactory to restrict all the numerical examples below to within $q = N_1 = N_2 = N_3 = 8$, which guarantees at least six significant figures for the numerical amplitude parameters.

4. Comparison with experiment

4.1. *Model tests*

Moonpool model tests were performed in the narrow-wave flume of the Department of Marine Technology, NTNU. This wave flume is 0.6 m wide, with water depth 1.03 m and total length 13.5 m. The flume is equipped with a single-flap wavemaker and a parabolic beach. The wavemaker is automatically controlled, and it moves to damp out incoming waves. A rectangular ship section with a moonpool undergoes small-amplitude regular oscillatory vertical (heave) motions. The focus is on the piston-mode resonance that occurs in the moonpool. The centre of the ship section is positioned 4.2 m away from the wavemaker.

The draught d and moonpool width L_1 were varied between tests. The width of the two rectangular shaped parts of the ship hull, B, was 0.36 m. The hull was made from plywood, and the corners were sharp. Vertical regular oscillatory motion was achieved by the use of a servo motor connected to a ball screw and rail system. Position steering was used for the servo motor. A Labview application generates the steering voltage signal at the analogue input of the servo-motor control loop. The set-up is shown in figure 2, where the servo-motor forcing mechanism is visible.

Figure 3 shows the positions of the wave probes, position gauges and accelerometers when the moonpool width and depth are both equal to 180 mm. A total of 12 wave

https://doi.org/10.1017/S002211200600440X Published online by Cambridge University Press

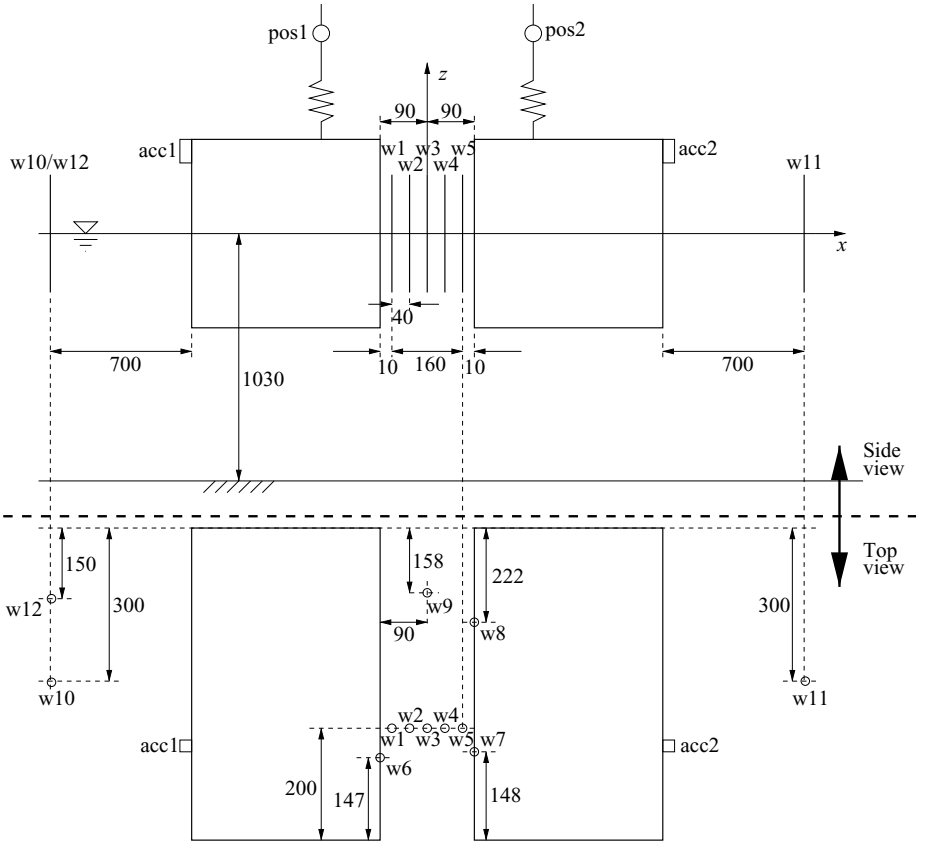


FIGURE 3. Instrumentation for a moonpool width and depth $L_1 = 180$ mm and $d = 180$ mm, respectively. All measurements are in mm.

probes were used, denoted w1–w12. Three of these, w6, w7 and w8, were made from parallel copper tape fixed to the ship section, while the rest consisted of two lengths of parallel wire and were Earth-fixed. The wires had diameter 3 mm, except for w1–w5 and w9, which had wire diameter 1.9 mm. The centre distance was about 10 mm for the wire probes, while the copper-tape probes had tape width 10 mm; the distance between the tapes was 10 mm. Wave probes w1–w5 were parts of the same unit. Both types of wave probe, copper-tape and wires, were capacitance probes. Because of the surface tension, the wire probes have an accuracy of the order of the wire radius, i.e. about 1 mm, when the instantaneous free surface, excepting the meniscus, is perpendicular to the wires. If the free surface is steep or curved, the accuracy may be lower. The copper-tape probes fixed to the ship-section walls have an accuracy limited by local effects between the free surface and the wall, exemplified by the thin films of water that stick to the wall a short while after the free surface has descended. Its position is measured by use of force rings with strain gauges attached by strings. In addition, the steering-system-position feed-back is sampled. The accelerometers were used to check for vibrations and could also be used as an extra means of position and velocity measurement. When the moonpool width was increased from $L_1 = 180$ mm to $L_1 = 360$ mm, the wave probes w1–w5 and w9 were kept in the moonpool centre, while the other sensors were moved outwards from the centre so that the relative distance to the side hulls was kept the same.

https://doi.org/10.1017/S002211200600440X Published online by Cambridge University Press

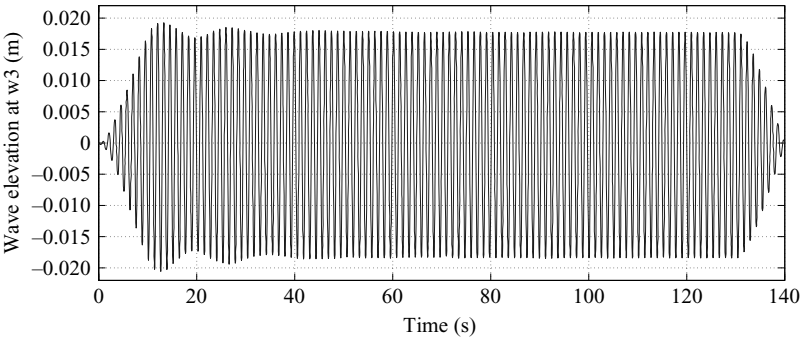


FIGURE 4. Free-surface elevation at wave probe w3 for $\eta_{3a} = 5$ mm, $L_1 = 180$ mm, $d = 180$ mm and $\sigma = 4.9637$ rad s^{-1}.

A Hottinger-Balwin MGC+ amplifier and data acquisition unit was used. The internal sampling frequency was 19.2 kHz, and a Butterworth low-pass 1 kHz filter was applied. Finally, the data was stored at 400 Hz. A typical test duration was 140 seconds, including the starting and finishing linear ramps on the forcing amplitude, each of which lasted for 10 seconds. After short transients, the experiments demonstrated, for a narrow forced-frequency range, clearly symmetric and two-dimensional piston-like $2\pi/\sigma$-periodic wave elevations in the moonpool. Figure 4 shows a typical recording of this elevation measured at probe w3. Note that if a trapped mode had existed we would have expected additional oscillations at the trapped-mode frequency. The start and end ramps are obvious, and clearly a steady state is reached. The automatically controlled wavemaker and parabolic beach prevent the reflection of radiated waves back onto the section. Fourier analysis was used to check that the dominating harmonics were equal to the forcing angular frequency σ. This provided an extra control on the experimental resonance frequency.

The typical progress of a test run was as follows. The ramp on the regular oscillatory heave-motion amplitude ensured a relatively short-lived transient for the response. Typically, the steady state was reached in less than 60 seconds. For most of the forcing frequencies, some initial beating occurred in the moonpool. The free-surface elevation inside the moonpool reached an absolute maximum and minimum in the middle, but the difference in level across the moonpool was not large. The minimum amplitude for radiated waves was observed for frequencies slightly higher than the frequency that results in the maximum free-surface elevation inside the moonpool. The measured steady-state free-surface elevation seemed quite sinusoidal. Viscous effects were obvious around the corners of the rectangular ship hulls, where tiny particles in the water visualized vortex shedding. This vorticity was especially evident when the free-surface-motion amplitude in the moonpool was large.

In summary, thinking in terms of our non-dimensional linear theoretical statement, the completed model tests for a wide range of forcing frequencies were performed with only three different geometric configurations, corresponding to the following dimensionless parameters.

Case 1: $h = 5.722\,22$, $d = 1$ and $B = 2$, with two forcing amplitudes, $\epsilon = 0.013\,889$ or $0.027\,778$;

Case 2: $h = 5.722\,22$, $d = 1.5$ and $B = 2$ with the same two forcing amplitudes;

Case 3: $h = 2.861\,11$, $d = 0.5$ and $B = 1$ with only one forcing amplitude, $\epsilon = 0.006\,94$.

https://doi.org/10.1017/S002211200600440X Published online by Cambridge University Press

The non-dimensional distance at which the wave amplitudes and phase shifts were measured was $w_p = 6.388\,89$ in cases 1 and 2 and $w_p = 3.4444$ in case 3.

All the experimental series detected a clear resonance about a certain non-dimensional frequency Λ_* for which the water elevations inside the moonpool reached their absolute maximum. The value of Λ_* was weakly dependent on the forcing amplitude. In cases 1 and 2, some isolated experiments were done for $0.013\,889 < \epsilon < 0.027\,78$ with forcing frequencies close to Λ_*. These confirmed the position of the resonance frequency Λ_* from (3.39).

4.2. *Comparison of theory and experiment*

In this subsection, we compare the theoretical predictions and experimental data for the following quantities:

• *the resonance frequency of the piston-like motions Λ_* associated in experiments with the maximum piston-like amplitude*. Theoretically, this frequency is computed as the limit of (3.39) as $q = N_1 = N_2 = N_3$ increases.

• *the steady-state amplitudes of the piston-like mode*, whose 'experimental' values for each fixed Λ were computed by numerical integration over the five probes w1–w5 shown in figure 3. In order to get the experimental values, the acquired time histories for the free-surface elevation at these probes as well as the vertical position measurement for the ship hulls were filtered at 10 Hz. Then the last 10 seconds of data before ramp-down were analysed, the local maxima stored and the mean and standard deviation of the maxima calculated. The standard deviation relative to the mean value was less than 3%. This implicitly confirmed that the measurement error was small. The normalized free-surface elevation was found as the ratio of the mean values of the free-surface elevation and the forcing amplitude. In our non-dimensional statement, the theoretical piston-like amplitudes are, using (2.3), defined as

$$\begin{aligned} M_a &= \Lambda \max_{t\in[0,2\pi]} \left| 2\int_{-1/2}^{0} \left.\frac{\partial\psi}{\partial t}\right|_{z=0} \mathrm{d}x \right| = \max_{t\in[0,2\pi]} \left| 2\int_{-1/2}^{0} \left.\frac{\partial\psi}{\partial z}\right|_{z=0} \mathrm{d}x \right| \\ &= \max_{t\in[0,2\pi]} \left| \mathscr{A}_1^{(1)} \cos t + \mathscr{A}_1^{(2)} \sin t \right|, \end{aligned} \tag{4.1}$$

where, accounting for the continuity of the fluid mass in subdomain IV,

$$\mathscr{A}_1^{(i)} = 2\int_{-1/2}^{0} w_3^{(i)}\,\mathrm{d}x, \quad i = 1, 2, \tag{4.2}$$

and, therefore,

$$P_a = \sqrt{\left(\mathscr{A}_1^{(1)}\right)^2 + \left(\mathscr{A}_1^{(2)}\right)^2}. \tag{4.3}$$

Explicit computational formulae for $\mathscr{A}_1^{(i)}$ following from our method are given in the online supplement. Because the experimental values are scaled by the forcing amplitude, an adequate comparison must impose $M_a := M_a/\epsilon$.

• *the wave amplitude at the far field*. Owing to (3.3), the net amplitude of the outgoing wave P_a is defined as follows:

$$\begin{aligned} P_a &= \max_{t\in[0,2\pi];x\in(-\infty,b)} \left| -\mathscr{A}_0^{(2)} \cos(\mathscr{K}(x+b)+t) + \mathscr{A}_0^{(1)} \sin(\mathscr{K}(x+b)+t) \right| \\ &= \sqrt{\left(\mathscr{A}_0^{(1)}\right)^2 + \left(\mathscr{A}_0^{(2)}\right)^2}, \end{aligned} \tag{4.4}$$

https://doi.org/10.1017/S002211200600440X Published online by Cambridge University Press

where

$$\mathscr{A}_0^{(i)} = \frac{\sinh \mathscr{K} h}{N_0} \int_{-h}^{-d} w_1^{(i)} \cosh(\mathscr{K}(z_0 + h))\, \mathrm{d}z_0, \quad i = 1, 2 \tag{4.5}$$

(approximate computational formulae for the $\mathscr{A}_0^{(i)}$ are presented in the online supplement). Comparisons involving the far-field wave amplitude require the vertical wave elevation at probe w11 ($x_{w_p} = -w_p - b$) to be scaled by the forcing amplitude. The dimensional distance between the hull and w11 was 700 mm. Accounting for the evanescent component, which may slightly affect the elevations at w11 (theoretically, by about 1%–4% for our experimental cases), the wave amplitude at x_{w_p} was computed from a more complicated formula than (4.4). Proceeding with integral representations gives

$$P_w = \max_{t\in[0,2\pi]} \left|\mathscr{A}_4^{(1)} \cos t + \mathscr{A}_4^{(2)} \sin t\right| = \sqrt{\left(\mathscr{A}_4^{(1)}\right)^2 + \left(\mathscr{A}_4^{(2)}\right)^2}, \tag{4.6}$$

where

$$\left.\begin{aligned} \mathscr{A}_4^{(1)} &= \mathscr{A}_2^{(1)} - \mathscr{A}_0^{(1)} \sin \mathscr{K} w_p - \mathscr{A}_0^{(2)} \cos \mathscr{K} w_p, \\ \mathscr{A}_4^{(2)} &= \mathscr{A}_2^{(2)} + \mathscr{A}_0^{(1)} \cos \mathscr{K} w_p - \mathscr{A}_0^{(2)} \sin \mathscr{K} w_p \end{aligned}\right\} \tag{4.7}$$

with

$$\mathscr{A}_2^{(i)} = \Lambda \int_{-h}^{-d} w_1^{(i)} \mathscr{G}_I(-w_p - b, 0; z_0)\, \mathrm{d}z_0. \tag{4.8}$$

Explicit approximate formulae for $\mathscr{A}_2^{(i)}$ are given in the online supplement.

- in case 3, *the steady-state amplitudes at the wave probes inside the moonpool* (w1–w5 at $x = x_{w_m} \in (-\frac{1}{2}, 0)$) are evaluated. Here, the experimental data were not able to clearly identity the piston-like steady amplitudes M_a. Theoretically, the steady non-dimensional amplitude at x_{w_m} is defined as

$$\begin{aligned} M_w &= \max_{t\in[0,2\pi]} \left|\Lambda \frac{\partial \psi_{IV}}{\partial t}(x_{w_m}, 0, t)\right| = \max_{t\in[0,2\pi]} |\Lambda \psi_{IV}(x_{w_m}, 0, t)| \\ &= \max_{t\in[0,2\pi]} \left|\mathscr{A}_3^{(1)} \cos t + \mathscr{A}_3^{(2)} \sin t\right| = \sqrt{\left(\mathscr{A}_3^{(1)}\right)^2 + \left(\mathscr{A}_3^{(2)}\right)^2}, \end{aligned} \tag{4.9}$$

where

$$\mathscr{A}_3^{(i)}(x_{w_m}) = \frac{\partial \varphi_{IV}^{(i)}}{\partial z}(x_{w_m}, 0) = \Lambda \varphi_{IV}^{(i)}(x_{w_m}, 0) = \int_{-1/2}^{0} w_3^{(i)} \mathscr{G}_{IV}(x_{w_m}, 0; x_0)\, \mathrm{d}x_0; \tag{4.10}$$

the computational formulae are given in the online supplement. As usual, these should be divided by ϵ for comparison with the non-dimensional model test data.

- *the theoretical and experimental phase shifts.* The experimental values arise from the time difference between the local maxima of the forcing $\eta_3 = -\eta_{3a} \cos \sigma t$ and those found in the recordings. Theoretical values of the phase shifts for the piston-like motions (θ_m), the wave elevation at w11 (θ_p) and the wave elevations at probes w1–w5 (θ_w) can easily be evaluated from the corresponding expressions (4.1), (4.6) and (4.9). Because the time-dependent quantities in (4.1), (4.6) and (4.9) represent non-dimensional vertical velocities (whose absolute maximum per period coincides with the elevations in our non-dimensional statements), the expressions within the modulus verticals should be compared with the input signal for the velocity on S_D,

https://doi.org/10.1017/S002211200600440X Published online by Cambridge University Press

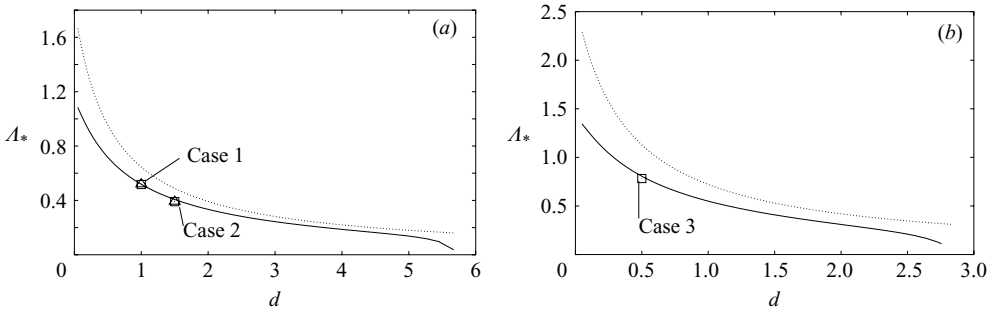


FIGURE 5. Theoretical prediction of the resonance frequency Λ_* (the root of (3.39)) versus d (solid line) and the estimate by Molin (2001) (dotted line). Panel (*a*) relates to cases 1 and 2 ($h = 5.722\,22$ and $B = 2$), but (*b*) relates to case 3 ($h = 2.861\,11$ and $B = 1$). The squares and triangles mark the experimental values of Λ_* for lower forcing amplitudes ($\epsilon = 0.013\,889$ in (*a*) and $\epsilon = 0.006\,944$ in (*b*)) and for larger forcing amplitudes ($\epsilon = 0.027\,78$), respectively.

i.e. with $\epsilon \sin t$. This implies that

$$\left.\begin{gathered} \mathscr{A}_1^{(1)} \cos t + \mathscr{A}_1^{(2)} \sin t = M_a \sin(t - \theta_m), \quad \mathscr{A}_2^{(1)} \cos t + \mathscr{A}_2^{(2)} \sin t = P_w \sin(t - \theta_p), \\ \mathscr{A}_3^{(1)} \cos t + \mathscr{A}_3^{(2)} \sin t = M_w \sin(t - \theta_w), \qquad \theta_m, \theta_p, \theta_w \in [0, 2\pi], \end{gathered}\right\} \tag{4.11}$$

where the phase shifts are computed by a standard trigonometric technique.

In addition, we calculated the added-mass and damping coefficients. Because measurements of vertical force on the hulls were not conducted, the hydrodynamic coefficients could not be compared. Theoretical values of the added mass and damping are derived and analysed in § 4.2.3.

4.2.1. *Resonance frequency*

The calculations confirmed that the maximum theoretical response (the local maximum of M_a from (4.1) as a function of Λ) coincides with the roots computed from (3.39). The solid lines in figure 5 show Λ_* versus d for two cases associated with our experiments. In addition, the figure includes the predictions by Molin (2001), which can be written as

$$\Lambda_* = \left(d + \frac{1}{\pi} \left(\frac{3}{2} + \ln \frac{b_*}{2} \right) \right)^{-1}, \tag{4.12}$$

where $b_* \geqslant b$ corresponds to the position of an artificial sink or source used in Molin's method (in both graphs, we have simply assumed that $b_* = b$; see figure 1 *b*). Although Molin's formula (4.12) is based on infinite-water-depth theory, implicitly assumes non-small B and, generally, gives results depending on b_*, which is *a priori* unknown, it reflects qualitatively well the behaviour of Λ_* versus d.

The theoretical and experimental piston-mode resonance frequencies compare well. The frequencies are almost equal in case 1 (figure 5*a*), while there are small differences in case 2 and 3, which are hardly visible in figure 5(*b*). The results of Molin (2001) are also illustrated. The discrepancy between Molin's results and ours increases when the draught is small relative to the moonpool width. Molin's prediction (4.12) gives larger Λ_* values, but these can be improved by a speculative manipulation of the artificial parameter b_*. Some practical recommendations on this point were given by Maisondieu *et al.* (2001).

https://doi.org/10.1017/S002211200600440X Published online by Cambridge University Press

4.2.2. *Amplitudes and phase shifts*

Measurements of the wave elevations in the moonpool and in the far field, away from the structure (henceforth, we focus only on measuring probe w11), make it possible to validate quantitatively the linear theoretical predictions. As we stated earlier, both experimental and theoretical values are scaled by the forcing amplitude. This implies that, owing to the linearity, the scaled theoretical amplitudes may simply be calculated by using the formal substitution $\epsilon = 1$ in (3.25), and these values are the same for different forcing amplitudes. In contrast, the scaled experimental wave amplitudes may change with the forcing. This is caused by various physical factors, including free-surface nonlinearity and vortex shedding, which are not accounted for by our linear-potential theory. The experimental and theoretical phase shifts θ_m and θ_p (see definitions (4.11)) were also evaluated. The experimental accuracy at the measured probes can be quantified. The relative error in the averaged values of the piston-like amplitudes is less than 3% for the case of maximum amplitude response. This was confirmed by two series in the case of figure 6(*a*) and three series in the case of figure 6(*c*) made, with the same forcing parameters, in the vicinity of the amplitude peak. These series were repeated from two to five times.

The experimental and linear theoretical behaviour of the scaled wave amplitudes is presented in figures 6(*a–d*), 7(*a–d*) and 8(*a–b*). These figures correspond to experimental cases 1–3. Note, that in case 3, when the experiments were made with a wider moonpool, the measuring probes w1–w5 remained at their original positions. In this case, the estimate of the piston-like amplitude from the recordings has limited accuracy. In terms of the non-dimensional statement only the vertical elevations at $x = -0.222\,22, -0.111\,11$ and 0 are known, but experimental data on what happened in $x \in [-1/2, 0.2222)$ are absent. Although the piston-like resonant motions yield almost flat profiles inside the moonpool, the difference in the elevations at different probes is generally speaking not negligible. Therefore, the comparison in case 3 will be done for the elevation at probe w3.

The results for cases 1 and 2 possess very similar features (figures 6 and 7). First of all, they demonstrate clearly a single resonance peak for the piston-like response so that the maximum theoretical values are of order about ten times the forcing amplitude. Further, the model tests conducted with lower forcing amplitudes approach the maximum piston-like amplitude, but the experimental value of the latter is less that in the linear inviscid theory. The agreement between the measured and theoretical values for both the piston-like and far-field amplitudes is satisfactory for smaller forcing amplitudes (figures 6 and 6*a*). Larger forcing amplitudes increase the discrepancy – compare figures 6(*a*) and 6(*b*) and figures 7(*a*) and 7(*b*). This is typical for nonlinear effects due to both flow separation at the corners and the free surface. The agreement with the experimental phase shifts in figures 6(*b*, *d*) is also not bad for both forcing amplitudes, especially for θ_m (note that to avoid jumps in the phase-shift function $\theta_m = \theta_m(\Lambda)$ in figures 6(*b*) and 6(*d*) we allowed θ_m to be larger than 2π in a small range of Λ).

In order to understand the nature of the resonance at Λ_* we have presented in panels (*e*) of figures 6 and 7 graphs of the amplitude components $\mathscr{A}_i^{(j)}$, $i = 0, 1$, $j = 1, 2$, scaled by ϵ. Owing to (4.3), the resulting piston-like amplitude is the mean square of the $\mathscr{A}_1^{(j)}$, $j = 1, 2$, whose absolute values reach maxima that are very close to each other and, as expected, M_a is maximal somewhere between these two maxima. The calculations confirm that this maximum value of M_a occurs at the resonance frequency Λ_*. One interesting point is that Λ_* coincides with the zero of the 'pressure'-based components of the outgoing wave, namely, $\mathscr{A}_0^{(2)} = 0$ at Λ_*. We have no reasonable

https://doi.org/10.1017/S002211200600440X Published online by Cambridge University Press

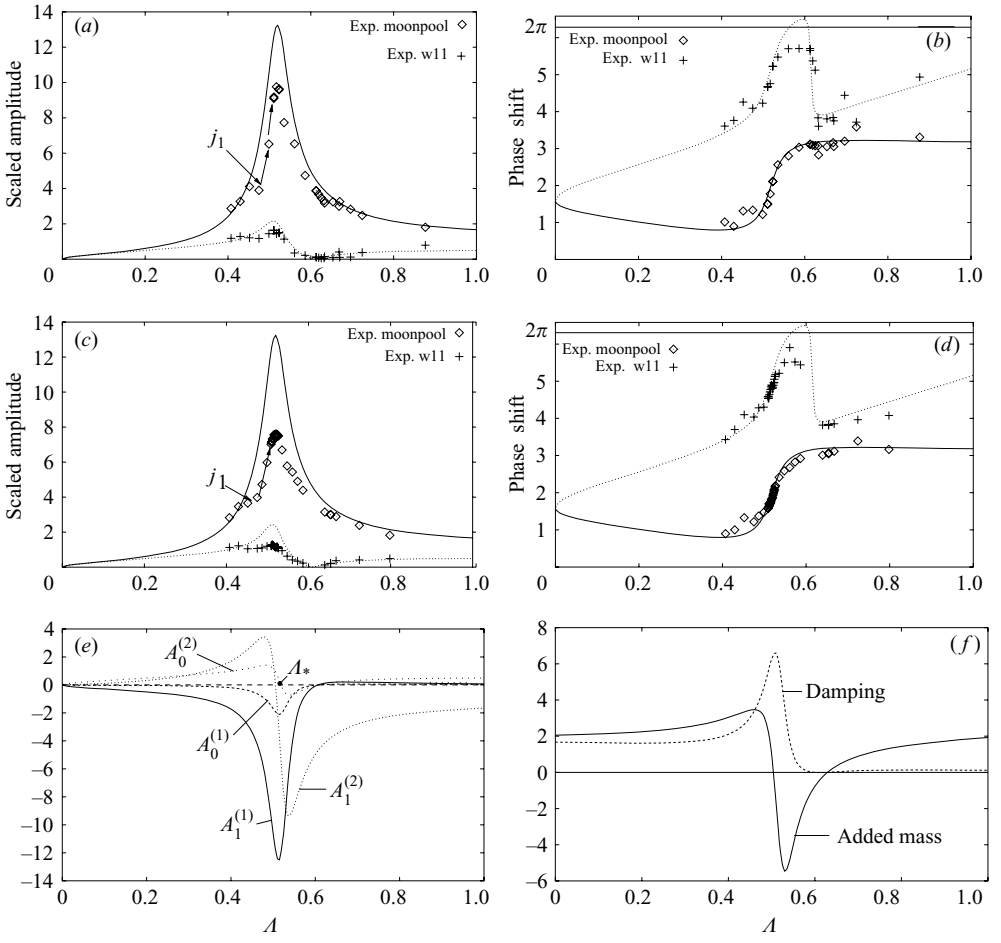


FIGURE 6. Case 1, for which $B=2$, $d=1$ and $h=5.722\,22$. Theoretical and experimental amplitudes of the piston-like motions M_a and the wave elevation at w11 P_w/ϵ, (scaled by the forcing amplitude), versus Λ are presented in (*a*), (*c*). The corresponding theoretical and experimental phase shifts θ_m and θ_p are given in (*b*), (*d*). Panels (*a*) and (*b*) give for comparison the results from theory and experiment for the experimental forcing amplitude $\epsilon=0.0138\,89$; however, (*c*) and (*d*) imply that $\epsilon=0.027\,778$. Panel (*e*) gives the theoretical behaviour of the scaled amplitudes $A_i^{(j)}=\mathscr{A}_i^{(j)}/\epsilon$, $i=0,1$, $j=1,2$. Panel (*f*) represents the theoretical prediction for the dimensionless added mass (A_{33} and the damping coefficients B_{33} defined by (4.16)–(4.18). The asymptotic limit $B_{33}\to 1.672\,16$ as $\Lambda\to 0$ is consistent with the formula (4.19).

physical explanation of this. In addition, panels (*f*) in figures 6 and 7 include the theoretical values of the non-dimensional added mass and the damping coefficient (4.17). The behaviour of the damping coefficient is linked with conservation of energy and it is discussed in § 4.2.3.

Cases 1 and 2 exhibit an interesting behaviour in the experimental data slightly away from the resonance. An example is the measured elevations around the point j_1 in figures 6(*a*) and 6(*c*). Because this behaviour is typical for both lower and higher forcing amplitudes, it cannot be explained by uncertainties in the measurements but looks like a nonlinear phenomenon. An additional reason for this is that, starting from j_1, the experimental response for the piston-like amplitude (as shown by the

https://doi.org/10.1017/S002211200600440X Published online by Cambridge University Press

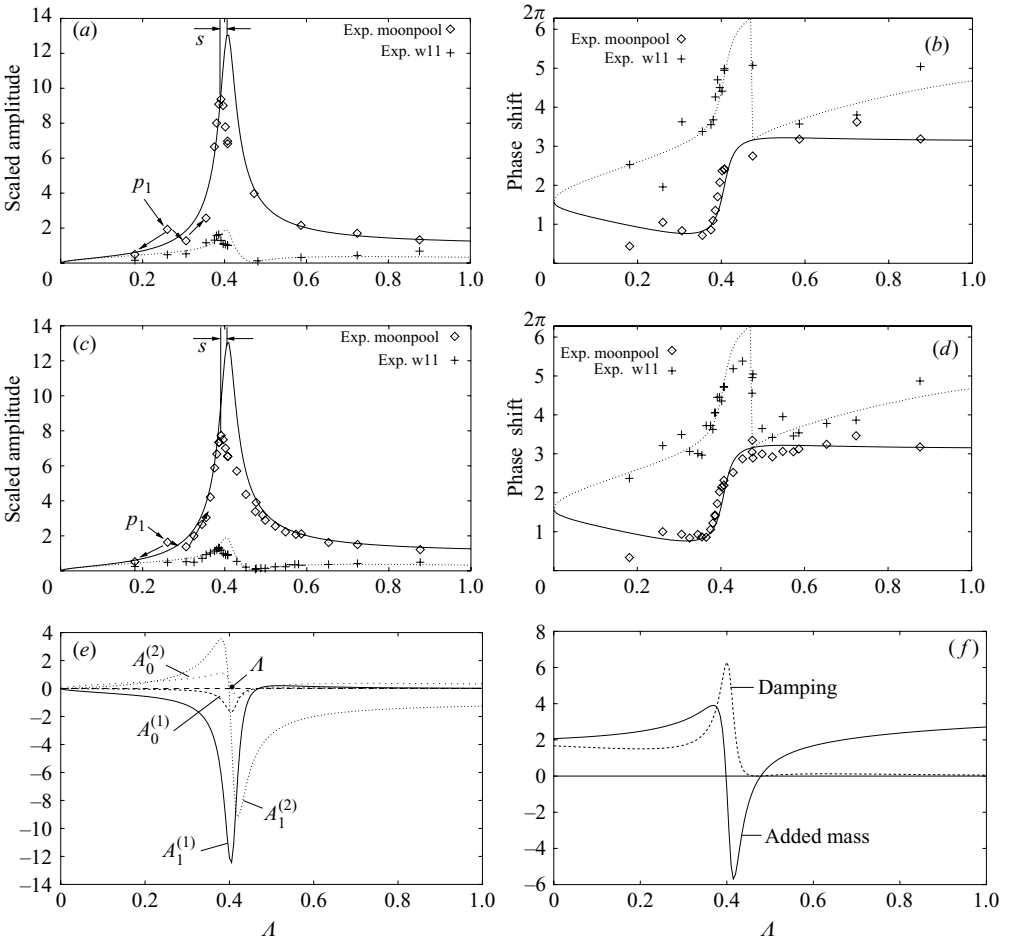


FIGURE 7. The same as figure 6, but for case 2 ($d = 1.5$).

arrows) becomes narrower than in the theoretical linear prediction. Furthermore, the experimental data from case 2 demonstrate a series of new discrepancies with regard to the theoretical predictions. First, a strange, non-smooth, behaviour, denoted p_1, is now detected from a single measurement away from the primary resonant zone. Once again, it is present for both the lower and higher forcing amplitudes. Second, the maximum experimental amplitude (a peak) is now slightly offset relative to the theoretical Λ_* by an amount s, so that comparing panels (a) in figures 6 and 7 gives the impression that either flow separation or a Duffing-like behaviour may occur in case 2. We will show later in the text that vortex shedding itself cannot be the reason.

Case 3 in figure 8 gives a comparison (dashed line) with the experimental values (the elevations at the middle probe w3). The solid line represents the theoretical piston-like amplitude. The difference between the solid and dashed lines is insignificant for the wave amplitudes (see figure 8a, where the theoretical predictions for M_a and M_w are very close to each other) and it is generally invisible in the graphs for the corresponding phase shifts (figure 8b is not able to distinguish them). In summary, cases 2 and 3 both show a drift s, of the maximum piston-like response, from the theoretical prediction to the experimental peak (compare panels a in figures 7 and

https://doi.org/10.1017/S002211200600440X Published online by Cambridge University Press

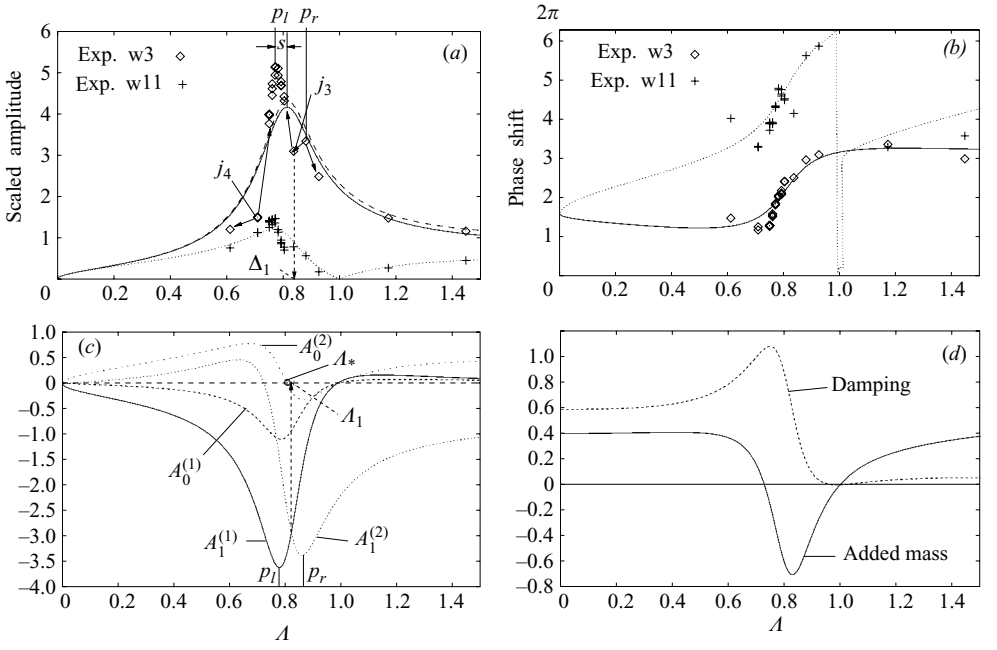


FIGURE 8. The same as figures 6(*a–f*) but for case 3, for which $B=1$, $d=0.5$, $h=2.861\,11$ and the experimental forcing amplitude $\epsilon=0.006\,944$. In addition, the dashed line in (*a*) corresponds to the scaled wave elevations M_w at w3 ($x_{w_m}=0$, in the middle of the moonpool) and may compared with the experimental results. Analogously, (*b*) represents by the dotted line the theoretical phase shift θ_w from (4.11). $B_{33}\to 0.5912$ as $\Lambda\to 0$.

8). However, while figures 6 and 7 indicate that, to some extent, agreement may be improved by accounting for a kind of damping, case 3, with a wider moonpool, in figures 8(*a*, *b*) is challenging. It demonstrates a behaviour of the maximum experimental piston-like amplitude in relation to linear theoretical predictions which cannot be clarified by an appeal to damping.

First of all, new features of the experimental data in case 3 are associated with point j_4 occurring to the left of the primary resonance Λ_*, and point j_3, occurring at Λ_*. These two points near the resonant Λ_* form a 'Bactrian camel' response (two humps) instead of an 'Arabian camel' response (one hump) in the theoretical data. Of special interest is the left-hand hump of the 'camel', which exceeds the theoretical maximum. Here we have numerous experimental data confirming this. Measured recordings corresponding to the key point j_3 will be discussed in the following text. A numerical analysis shows that the positions of Λ, p_l and p_r, where the absolute values of $\mathscr{A}_1^{(1)}$ and $\mathscr{A}_1^{(2)}$ reach their maxima, coincide with the experimental Λ values at which the experimental data have two local maxima ('humps'). The net amplitude M_a is the mean square of the sine or cosine amplitudes $\mathscr{A}_1^{(1)}$ and $\mathscr{A}_1^{(2)}$ in figure 8(*c*). When obtaining steeper maxima for $|\mathscr{A}_1^{(1)}|$ and $|\mathscr{A}_1^{(2)}|$ due to nonlinearity or a damping, generally speaking one obtains a camel-like curve for M_a.

An illustration showing explicity that the resonance phenomenon in case 3 are characterized by the influence of nonlinearity and, as a consequence, by amplification of the higher harmonics, follows from the Fourier analysis in figure 9. The emphasis is on the point j_3. Here, panels (*a*) and (*b*) give recordings at w1 and w5 for case 1 ($\Lambda=0.5357$ or $\sigma/2\pi=0.86$ Hz) and periodic elevations in case 3 ($\Lambda=0.8041$ or

https://doi.org/10.1017/S002211200600440X Published online by Cambridge University Press

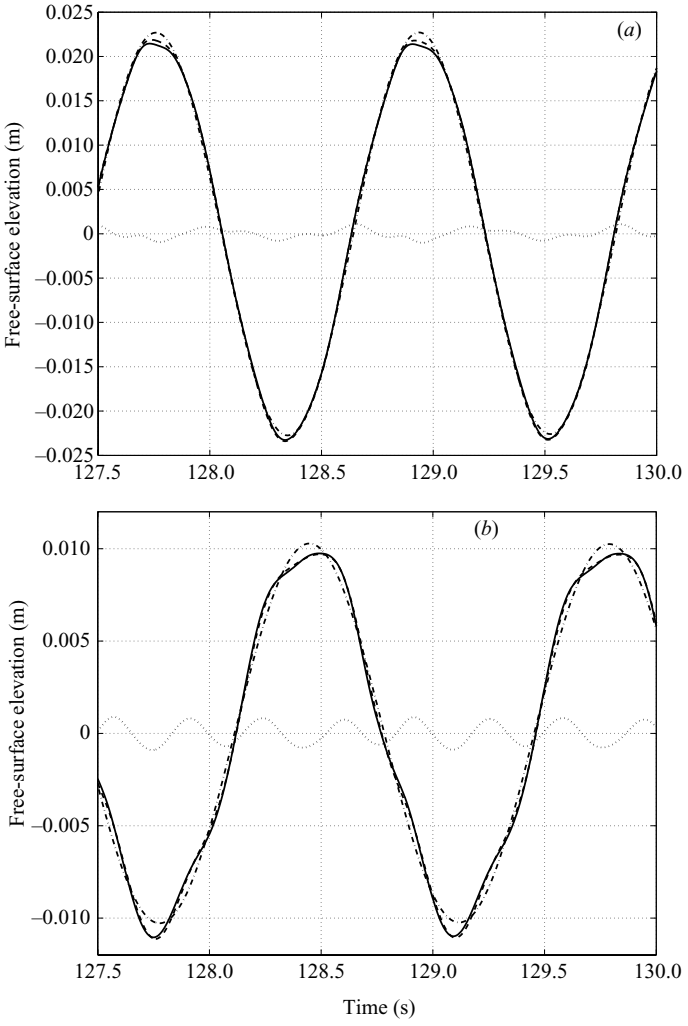


FIGURE 9. Dimensional steady-state elevations at w1 (solid line), w5 (dashed line) and their Fourier filtering in the range 0.5–1.3 Hz (dot-and-dashed line) and 1.3–10 Hz (dotted line). (*a*) Case 1 with $\Lambda = 0.5357$ (0.86 Hz) and (*b*) corresponds to j_3 in figure 8 (*a*) with $\Lambda = 0.8041$ (0.745 Hz).

$\sigma/2\pi = 0.745$ Hz, the point j_3), respectively. The contributions of the filtered lower and higher harmonics at w5 are also presented. Figure 9(*b*) demonstrates clearly periodic but non-sinusoidal signals, which are contributed by higher harmonics than in figure 9(*a*). The dominating higher harmonics is four times larger than the forcing frequency. A logical explanation of these higher harmonics may be an internal (secondary) resonance between the piston-like mode at $\Lambda_* = 0.8041$ and a sloshing mode characterized by non-dimensional resonant frequencies Λ_i, $i \geqslant 1$. The piston-like mode may create only a parametric-type resonance for the sloshing modes and the resonant sloshing frequencies are quite a lot larger than the lowest piston-like Λ_*. This means that the secondary resonance, in terms of a nonlinear theory which produces $l\sigma$, $l = 1, 2, \ldots$ harmonics, is predictable when $l\sigma/\sigma_i$, $l \geqslant 1$, $i \geqslant 1$ is an integer. Thinking in terms of the lowest l and i and using estimates of the

https://doi.org/10.1017/S002211200600440X Published online by Cambridge University Press

resonant sloshing frequencies by Molin (2001), we find that $l\sigma/\sigma_i \approx \sqrt{l/2i}$ for Λ_* in case 3. Possible 'resonance' combinations are $l=2, i=1$, $l=4, i=1$, $l=4, i=2$ etc. Special studies are needed to select an actual secondary resonance from these combinations.

4.2.3. *Energy-conservation rule and asymptotic behaviour as* $\Lambda \to 0$

According to Newman (1977) and Faltinsen (1990), the time derivative of the total dimensional energy of the entire moonpool can be written for our Oz-symmetric flows as

$$\frac{\mathrm{d}E}{\mathrm{d}\bar{t}} = 2\int_{\bar{S}_B} (\bar{p}-\bar{p}_0)\left(-\frac{\partial\bar{\psi}}{\partial\bar{z}}\right)\mathrm{d}\bar{x} - 2\rho\int_{\bar{S}_{-\infty}} \frac{\partial\bar{\psi}}{\partial\bar{t}}\frac{\partial\bar{\psi}}{\partial\bar{\nu}}\,\mathrm{d}\bar{z}$$

where $\bar{\psi}$, the spatial coordinates and the time are dimensional, ρ is the fluid density, p is the hydrodynamic pressure, p_0 is the atmospheric pressure, the normal vector $\bar{\boldsymbol{\nu}}$ is directed into the fluid volume and the auxiliary vertical line $\bar{S}_{-\infty}$ is located far away from the moonpool.

Thinking in terms of the value of $\mathrm{d}E/\mathrm{d}\bar{t}$ averaged over the period $T=2\pi/\sigma$, we can derive the following expression:

$$\left\langle \frac{\mathrm{d}E}{\mathrm{d}\bar{t}} \right\rangle = \frac{1}{T}\int_0 \frac{\mathrm{d}E}{\mathrm{d}\bar{t}}\,\mathrm{d}\bar{t} = 2\rho L_1^4\sigma^3\epsilon^2(\mathscr{I}_i - \mathscr{I}_o) = 0, \tag{4.13}$$

where the non-dimensional finite quantities $\mathscr{I}_i$ and $\mathscr{I}_o$ in the parentheses are responsible for the time-averaged energy income (due to forcing) and damping (due to outgoing wave), respectively. These are defined via the following expressions:

$$\mathscr{I}_i = -\frac{1}{2\epsilon}\int_{-b}^{-1/2} \varphi_{II}^{(1)}(x,-d)\,\mathrm{d}x, \quad \mathscr{I}_o = \frac{N_0}{2\epsilon^2\mathscr{K}\sinh^2\mathscr{K}h}\left(\left(\mathscr{A}_0^{(1)}\right)^2 + \left(\mathscr{A}_0^{(2)}\right)^2\right), \tag{4.14}$$

where the amplitudes $\mathscr{A}_0^{(i)}$ are defined by (4.5) and the computational formula for $\mathscr{I}_i$ is given in the online supplement. Note that $\varphi_{II}^{(1)} \sim \epsilon$ and $\mathscr{A}_0^{(i)} \sim \epsilon$ and, therefore, the presence of the small quantity ϵ in (4.14) is necessary to keep $\mathscr{I}_i$ and $\mathscr{I}_o$ finite.

The energy-conservation rule for steady-state waves requires $\mathscr{I}_i = \mathscr{I}_o$. This equality has been strictly controlled in all our computations. When $q=N_1=N_2=N_3=8$, it has always been satisfied to within a relative error 10^{-7}. This is consistent with the mean precision of the method.

Another important point relates to the asymptotic behaviour of the amplitude parameters as $\Lambda \to 0$. Direct computation showed that both the piston-like amplitudes M_a and the amplitudes of the outgoing waves P_a tend to zero in this limit. This fact does not follow directly from the boundary problem (2.2) with $\Lambda=0$ because, clearly, the rigid-free-surface condition is correct in the near field but not at infinity.

By fixing the geometric parameters h, d and B as finite, accounting for the fact that $\mathscr{K} = \sqrt{\Lambda/h} + o(\sqrt{\Lambda})$, $N_0 = h + O(\Lambda)$ and assuming that Λ_* is far from zero, we may deduce that the mean-square norms of $w_j^{(i)}$ are finite. This justifies the applicability of asymptotic analysis to the system of integral equations (3.21), which in this case applies to finite kernels defined on finite domains. By implementing

https://doi.org/10.1017/S002211200600440X Published online by Cambridge University Press

standard asymptotic expansions in (3.21), one gets the following solution:

$$\left.\begin{aligned}
&\mathscr{A}^{(1)}_{-1} = \mathscr{A}^{(1)}_{-2} = -\frac{\epsilon\left(b-\frac{1}{2}\right)}{\sqrt{h\Lambda}} + \epsilon O(1), \quad \mathscr{A}^{(2)}_{-1} = \mathscr{A}^{(2)}_{-2} = \epsilon O(1),\\
&\mathscr{A}^{(1)}_{1} = 2\int_{-1/2}^{0} w_3^{(1)}(x_0)\,\mathrm{d}x_0 = 2\int_{-h}^{-d} w_2^{(1)}(z_0)\,\mathrm{d}z_0 = \frac{\epsilon\left(b-\frac{1}{2}\right)}{\sqrt{h}}\sqrt{\Lambda} + \epsilon o(\sqrt{\Lambda}),\\
&\mathscr{A}^{(2)}_{1} = 2\int_{-1/2}^{0} w_3^{(2)}(x_0)\,\mathrm{d}x_0 = 2\int_{-h}^{-d} w_2^{(2)}(z_0)\,\mathrm{d}z_0 = \epsilon o(\sqrt{\Lambda}),\\
&\mathscr{A}^{(1)}_{0} = \frac{\epsilon\left(b-\frac{1}{2}\right)}{2h}\Lambda + \epsilon o(\Lambda), \quad \mathscr{A}^{(2)}_{0} = \epsilon\left(b-\frac{1}{2}\right)\sqrt{\frac{\Lambda}{h}} + \epsilon o(\Lambda),
\end{aligned}\right\} \tag{4.15}$$

which, as we can see, governs only the fluxes over the transmission lines. Higher-order approximations will describe the $w_j^{(i)}$ as functions of spatial coordinates.

Solution (4.15) confirms that both the outgoing wave amplitude P_a and the piston-like M_a amplitude, defined by (4.4) and (4.1), respectively, tend to zero as $\sqrt{\Lambda} \to 0$. An arbitrary constant which must be added to the solution in this limit due to vanishing Λ (it is represented by $\mathscr{A}^{(i)}_{-j}$, $i, j = 1, 2$, in the corresponding subdomains) comes from the far-field solution and tends to infinity as $\Lambda \to 0$.

Finally, we considered the added mass $\bar{A}_{33}$ and damping coefficient $\bar{B}_{33}$ for the catamaran, i.e. both the hulls were included. Accounting for the Oz-symmetry derives their dimensional values as

$$\bar{A}_{33} = 2\rho L_1^2 \int_{-b}^{-1/2} \frac{1}{\epsilon}\varphi^{(2)}_{II}(x,-d)\,\mathrm{d}x \quad \text{and} \quad \bar{B}_{33} = -2\rho L_1^2\sigma \int_{-b}^{-1/2} \frac{1}{\epsilon}\varphi^{(1)}_{II}(x,-d)\,\mathrm{d}x, \tag{4.16}$$

where the $\varphi^{(i)}_{II}$, $i = 1, 2$, are non-dimensional and defined by (3.8).

By normalizing $\bar{A}_{33}$ and $\bar{B}_{33}$ as

$$A_{33} = \frac{\bar{A}_{33}}{2\rho L_1^2}, \quad B_{33} = \frac{\bar{B}_{33}}{2\rho L_1^2\sqrt{g/L_1}}, \tag{4.17}$$

we obtain finite non-dimensional values, which are presented in figures 6(*f*), 7(*f*) and 8(*d*) as a function of Λ. The computational formula for A_{33} is presented in the online supplement, but, owing to the energy-conservation rule and (4.14), the non-dimensional damping coefficient is equal to

$$B_{33} = 2\sqrt{\Lambda}\,\mathscr{I}_o. \tag{4.18}$$

Physically, this means that the damping in our case is associated with the non-dimensional energy flux of the outgoing wave.

It is well-known (Bai & Yeung 1974) that the two-dimensional added mass $\bar{A}_{33}$ in heave motion at finite depth approaches a constant as $\sigma \to 0$. Our results confirm this. The corresponding behaviour of B_{33} has been analysed by Kan (1977) and McIver & Linton (1991). By using the asymptotic solution (4.15), one obtains

$$\lim_{\Lambda\to 0} B_{33} = \frac{B^2}{\sqrt{h}}, \tag{4.19}$$

which is consistent with Kan (1977). It was used by us as a control and always gave the right predictions, shown in figures 6(*f*), 7(*f*) and 8(*d*).

One interesting point is that the limit does not depend on the draught d. This follows from (4.19) and is confirmed by numerical experiments. In addition, because the solutions of the problem are weakly affected by h for certain $h > h_*$, we can take

https://doi.org/10.1017/S002211200600440X Published online by Cambridge University Press

$h \to \infty$. This means that B_{33} vanishes as it should do for the infinite-water-depth case. One should note that the dimensional expression for the limit of the damping coefficient is

$$\lim_{\sigma \to 0} \bar{B}_{33} = 2\rho B^2 \sqrt{\frac{g}{h}} \tag{4.20}$$

(here, all the values are dimensional), so that it is independent of L_1. This makes it possible to take $L_1 \to 0$ and get the result for the damping coefficient of a single rectangular free-surface-piercing body performing a harmonic heave motion.

Actually, we can show that the limit (4.20) with $2B$ as the waterplane length is true for any two-dimensional mono- and multihull body that is symmetric about the centre-plane. This follows by using matched asymptotic expansions, in which the rigid-free-surface condition applies in the near field. The outer expansion of the near-field solution represents a uniform flow following from the continuity of the fluid mass. The flow at infinity in the far-field solution follows from matching with the near-field solution and by applying a wavemaker solution similar to (3.3), with the wavemaker at the centre-plane. To obtain the desired result, the resulting wave amplitude at infinity should be combined with the energy-conservation condition.

5. Effect of vortex shedding

5.1. *Discrete-vortex method and results of Graham (1980)*

The discrete-vortex method assumes the vorticity to be concentrated in thin boundary layers and free-shear layers. Diffusion of the vorticity in the free-shear layers is neglected. This is appropriate at high Reynolds numbers. The method is best suited when the separation points are clearly defined at sharp edges. Details of the boundary-layer flow are then unnecessary. However, the vorticity is generated in the boundary layer and fed into the free shear layer. This is mathematically accounted for by using a generalized Kutta–Joukowski condition at the separation points. The free-shear layers are approximated by discrete vortices that are convected with the fluid. The forces on the body can be obtained by integrating the pressure either expressed via the unsteady Bernoulli equation or directly by means of the Blasius equation. Comprehensive reviews of the literature may be found in Graham (1980) and Downie *et al.* (1988) as well as in the books by Lewis (1991) and Sarpkaya & Isaacson (1981).

When the ambient oscillatory flow is harmonic with circular frequency σ and the Keulegan–Carpenter number $K_c = 2\pi\hat{U}/(\sigma L)$ is small (here $\hat{U}$ is the ambient flow-velocity amplitude and L is a characteristic body length), further simplifications may be made in modelling the viscous-flow effect. If K_c is small, the shed vorticity is concentrated near the sharp corners. Each of the local edge flows becomes analogous to the flow past an infinite wedge. The non-separated global flow provides inflow conditions to the local edge flows. However, there is no direct interaction between the vortices at the different local edge flows. The total vortex-induced force on the body is a straightforward sum of the local vortex-induced forces due to the local edge flows.

The discrete vortex analysis of shedding from an isolated edge was carried out by Graham (1977, 1980) by using a conformal mapping technique. He assumed a stable and regular oscillatory process with small K_c as observed in the experiments for sharp-edged bluff cylinders by Singh (1979). An oscillatory ambient flow past an infinite wedge of internal angle $\alpha < \pi$, with complex velocity amplitude $\hat{\mathscr{U}} = \mathrm{e}^{\mathrm{i}\beta_0}\hat{U}$, where β_0 defines the ambient flow direction past the body, was considered. Our objective was to

https://doi.org/10.1017/S002211200600440X Published online by Cambridge University Press

apply Graham's results. The needed length scales and inflow conditions in Graham's formulae for the vortex-induced force must be properly described.

First, Graham gave the formula for the complex force in terms of the strengths $\Upsilon_i(t)$ and positions $\zeta_i(t)$ of N vortices in the auxiliary complex plane ζ that is a conformal transformation of the original complex flow plane Z:

$$\mathscr{F}_v = -\mathrm{i}\rho \frac{\mathrm{d}}{\mathrm{d}t}\left[\sum_{n=1}^{N} \Upsilon_n(t)(\zeta_n(t) - \bar{\zeta}_n(t))\right] = \mathrm{e}^{\mathrm{i}\alpha_0}\ F_v. \tag{5.1}$$

Here α_0 determines the direction of the force and the $\bar{\zeta}_n$ are complex conjugates (in the case of the outer part of a circle, the $\bar{\zeta}_n$ must be replaced by the image points inside the circle).

The auxiliary flow plane ζ consists of either a half-plane or the outer part of a circle. As a consequence the singular local ambient flow at the sharp edge becomes regular, and the ambient flow velocity is governed in ζ by

$$\mathscr{U}(t) = \mathrm{e}^{\mathrm{i}\beta_0}\ U(t) = \hat{\mathscr{U}} \sin(\sigma t + \theta) = \mathrm{e}^{\mathrm{i}\beta_0}\ \hat{U} \sin(\sigma t + \theta) \tag{5.2}$$

($\beta_0 = 0$ when the transformed fluid plane coincides with the lower half-plane). Later, Graham showed that the vortex-induced force acts perpendicularly to the bisector of the wedge, and he presented a generalized Morison formula for the bisectoral vortex-induced force F_v:

$$F_v = \tfrac{1}{2}\rho \hat{U}^2 L K_c^{(3-2\lambda)/(2\lambda-1)} \Psi(t), \tag{5.3}$$

where ρ is the fluid density and $\lambda = 2 - \alpha/\pi$. The dimensionless function Ψ is approximated as

$$\Psi(t) = \bar{a} \sin(\sigma t + \theta)|\sin(\sigma t + \theta)| + \bar{b} \cos(\sigma t + \theta), \tag{5.4}$$

where the values $\bar{a}$ and $\bar{b}$ depend on α, e.g. $\bar{a} = 1.57$ and $\bar{b} = -0.16$ for our studied case, $\alpha = \pi/2$.

The formula (5.3) needs a characteristic length scale L. For an infinite wedge, L defines the dimensional relationship between the real and transformed planes. It is the distance, from the edge to a point Z_p in the original flow plane, that is equal to the distance from the origin of the corresponding point ζ_p in the transformed plane, i.e. $|Z_p| = |\zeta_p| = L$. Further, the use of (5.3) suggests matching the flow at the edge of an infinite wedge to the inner region of an oscillatory ambient flow (amplitude $\hat{U}$ and frequency σ) past a finite body with the same edge angle. The ambient-flow velocity is singular in the original plane and, therefore, the matching is carried out in the transformed plane in order to avoid the singularity. This relates the length scale L to $\hat{U}$ and σ. The complex potential for the attached (non-separated) flow round a wedge (mapped to a half-plane) is

$$W_0(\zeta, t) = U(t)\zeta, \tag{5.5}$$

where the real part of $U(t)$ is the original velocity scale in (5.2). As shown by Downie *et al.* (1988), the matching can be done by means of a Schwartz–Christoffel transformation. The latter computes the needed length scale L at the edge as the main asymptotic term

$$Z = \mathrm{e}^{\mathrm{i}\alpha_1} L^{1-\lambda} \zeta^{\lambda} \tag{5.6}$$

of the transformation in the vicinity of the corner point. Here α_1 depends on the angular position of the wedge. The details will be discussed extensively in the next section.

https://doi.org/10.1017/S002211200600440X Published online by Cambridge University Press

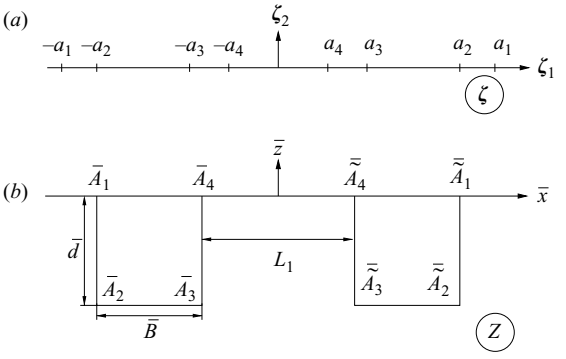


FIGURE 10. (*a*) The original complex flow plane Z formed in the lower subplane by the Ox-axis and two ship hulls and (*b*) the transformed flow domain appearing as the lower half-plane formed by the $O\zeta_1$-axis. The Schwartz–Christoffel transformation of these domains is defined by (5.7), where $a_1 = a_2 + a_3 - a_4$.

5.2. *Local velocity field in the transformed plane*

5.2.1. *Conformal transformation*

A Schwartz–Christoffel transformation is used to map the fluid flow in the original fluid domain Z to an auxiliary lower half-plane ζ, as shown in in figure 10:

$$Z = \int_0^{\zeta} \mathscr{H}(\xi, a_1, a_2, a_3, a_4)\,\mathrm{d}\xi, \quad \mathscr{H} = \left(\frac{(\xi^2 - a_2^2)(\xi^2 - a_3^2)}{(\xi^2 - a_1^2)(\xi^2 - a_4^2)} \right)^{1/2}, \tag{5.7}$$

where $a_1 = a_2 + a_3 - a_4$ with $0 < a_4 < a_3 < a_2$. Further, the a_i are uniquely determined by the moonpool width and the side-hull beam and draft on solving the system

$$\int_0^{a_4} \mathscr{H}\,\mathrm{d}\xi = \frac{L_1}{2}, \quad \int_{a_4}^{a_3} \mathscr{H}\,\mathrm{d}\xi = -\mathrm{i}\bar{d}, \quad \int_{a_3}^{a_2} \mathscr{H}\,\mathrm{d}\xi = \bar{B}, \tag{5.8}$$

where $a_1 = a_2 + a_3 - a_4$.

Concentrating on the corner points $\bar{A}_2$ and $\bar{A}_3$ in the Schwartz–Christoffel transformation (5.7) and using the l'Hôpital rule gives

$$\left.\begin{aligned} Z - \bar{A}_2 &= L_{A_2}^{-1/2}(\zeta + a_2)^{3/2}, \quad \zeta \to -a_2, \\ Z - \bar{A}_3 &= e^{\mathrm{i}\pi/2} L_{A_3}^{-1/2}(\zeta + a_3)^{3/2}, \quad \zeta \to -a_3, \end{aligned}\right\} \tag{5.9}$$

where $\bar{A}_2 = -L_1 - \bar{B} - \mathrm{i}\bar{d}$, $\bar{A}_2 = -L_1 - \mathrm{i}\bar{d}$ and, as a result,

$$L_{A_2} = \frac{9(a_2^2 - a_4^2)(a_1^2 - a_2^2)}{8a_2(a_2^2 - a_3^2)}, \quad L_{A_3} = \frac{9(a_1^2 - a_3^2)(a_3^2 - a_4^2)}{8a_3(a_2^2 - a_3^2)} \tag{5.10}$$

define the needed length scales at $\bar{A}_2$ and $\bar{A}_3$, respectively. In the limit $L_1 \to \infty$, this result is consistent with that of Downie *et al.* (1988), who analysed the vortex shedding due to a single rolling hull.

5.2.2. *Local flows without vortices*

The complex potential W_0 for the original velocity field without vortices in the plane Z is determined by (3.27). The local representation transforms to the plane ζ

https://doi.org/10.1017/S002211200600440X Published online by Cambridge University Press

by using

$$\frac{\mathrm{d}W_0}{\mathrm{d}\zeta} = \frac{\mathrm{d}W_0}{\mathrm{d}Z}\frac{\mathrm{d}Z}{\mathrm{d}\zeta}.$$

Accounting for (3.27) and (5.9) gives, in a small neighbourhood of $\bar{A}_2$ and $\bar{A}_3$,

$$\left.\frac{\mathrm{d}W_0}{\mathrm{d}\zeta}\right|_{\mathrm{at}\bar{A}_2} = \left[T_1^{(2)}(t)\ \tfrac{3}{2}L_{A_2}^{-1/3}\right] + \left[e^{-\mathrm{i}\pi/2}\ \tfrac{3}{2}L_{A_2}^{-1/2}\eta_{3a}\sigma\sin\sigma t\right](\zeta+a_2)^{1/2} + O(|\zeta+a_2|), \tag{5.11a}$$

$$\left.\frac{\mathrm{d}W_0}{\mathrm{d}\zeta}\right|_{\mathrm{at}A_3} = \left[T_1^{(3)}(t)\tfrac{3}{2}L_{A_3}^{-1/3}\right] + \left[\tfrac{3}{2}L_{A_3}^{-1/2}\eta_{3a}\sigma\sin\sigma t\right](\zeta+a_3)^{1/2} + O(|\zeta+a_3|), \tag{5.11b}$$

i.e. the dominating terms in the transformed plane are as follows:

$$W_0(\zeta,t) \approx U^{(3)}(t)\,\zeta, \quad \zeta\to -a_3, \qquad W_0(\zeta,t)\approx U^{(2)}(t)\,\zeta, \quad \zeta\to -a_2, \tag{5.12}$$

where

$$U^{(k)}(t) = \tfrac{3}{2}L_{A_k}^{-1/3}T_1^{(2)}(t) = \underbrace{\tfrac{3}{2}L_{A_k}^{-1/3}L_1^{4/3}\sigma\tfrac{2}{\sqrt{3}}\gamma\sqrt{\left(\alpha_1^{(k-1,1)}\right)^2+\left(\alpha_1^{(k-1,2)}\right)^2}}_{\hat{U}^{(k)}}\ \sin(\sigma t+\theta_{A_k}). \tag{5.13}$$

An important point is that both the coefficients $\alpha_1^{(i,j)}$ and the phase lags $\theta_{A_2},\theta_{A_3}$ are obtained in § 3.2.2 from our global inviscid solution without vortices. This means that using (5.13) implies that all the boundary conditions (including those on the free surface) are satisfied. As a consequence, since the ambient flows at $\bar{A}_2$ and $\bar{A}_3$ computed via (5.13) are not equivalent and, in general, $\hat{U}^{(3)}\not\equiv\hat{U}^{(2)}$ and $L_{A_2}\neq L_{A_3}$, the Keulegan–Carpenter numbers are different for the local flows at each edge, i.e. they are given by

$$K_c^{(k)} = \frac{\hat{U}^{(k)}2\pi}{\sigma L_{A_k}}, \quad k=2,3. \tag{5.14}$$

5.2.3. *The local flows due to vortex shedding*

The complex velocity potential W for the local flow at an edge consists of the sum of W_0 and discrete vortices shed from either $\bar{A}_2$ or $\bar{A}_3$. There are N_2 and N_3 vortices localized in the neighbourhoods of $-a_2$ and $-a_3$, respectively. Furthermore, $\zeta_n^{(2)}(t)$, $\Upsilon_n^{(2)}(t)$, $n=1,\ldots,N_2$ and $\zeta_n^{(3)}(t)$, $\Upsilon_n^{(3)}(t)$, $n=1,\ldots,N_3$ are given functions whose appearance and time evolution are related to direct simulations by the generalized Kutta–Joukowski condition, as elaborated by Graham (1980). Accounting for the dominating term (5.12), the complex velocity potential in the vicinity of a corner can be presented as

$$W|_{\mathrm{at}\bar{A}_k} = U^{(k)}(t)\zeta + \sum_{n=1}^{N_k}\frac{\mathrm{i}\Upsilon_n^{(k)}}{2\pi}\left[\log\left(\zeta-\zeta_n^{(k)}\right)-\log\left(\zeta-\bar{\zeta}_n^{(k)}\right)\right], \quad k=2,3. \tag{5.15}$$

5.3. *Vortex-induced vertical force*

Owing to the Oz-symmetry of the velocity field, the complex force on the bottoms of the two hulls follows from doubling the force acting on the bottom of a single hull. The linear, dominating, term of the complex force is

$$\mathscr{F} = 2\mathrm{i}\int_{\bar{S}_D}\mathscr{P}\,\mathrm{d}Z, \quad \mathscr{P} = -\rho\frac{\partial W}{\partial t}, \tag{5.16}$$

https://doi.org/10.1017/S002211200600440X Published online by Cambridge University Press

where $\bar{S}_D$ is the bottom area of a side-hull. The vortex-induced complex-pressure contribution is

$$\mathscr{P}_v = \mathscr{P}_v^{(2)} + \mathscr{P}_v^{(3)}, \qquad \mathscr{P}_v^{(k)} = -\frac{\rho \mathrm{i}}{2\pi}\frac{\mathrm{d}}{\mathrm{d}t}\sum_{n=1}^{N_k} \Upsilon_n^{(k)}(t)\log\left(\frac{\zeta-\zeta_n^{(k)}(t)}{\zeta-\bar{\zeta}_n^{(k)}(t)}\right), \quad k=2,3. \tag{5.17}$$

$\mathscr{P}_v$ is real on the interval $\zeta \in (-a_2, -a_3)$ and pure imaginary for $\zeta \in (-a_1, a_2) \cup (-a_3, a_4)$.

Using (5.17) gives the complex vortex-induced force on the two linked hulls. Its vertical component (pure-imaginary part) is the sum of the vortex-induced forces at the two edges, i.e.

$$\mathscr{F}_v = 2\big(\mathscr{F}_v^{A_2} + \mathscr{F}_v^{A_3}\big), \qquad \mathscr{F}_v^{A_k} = \mathrm{i}\int_{\bar{A}_2}^{\bar{A}_3} \mathscr{P}_v^{(k)}\,\mathrm{d}Z = e^{\mathrm{i}\pi/2}\,F_v^{A_k}, \quad k=2,3.$$

Using (5.17) gives

$$F_v^{A_k} = -\rho \mathrm{i}\frac{\mathrm{d}}{\mathrm{d}t}\sum_{n=1}^{N_k}\Upsilon_n^{(k)}(t)J_{A_k}\big(\zeta_n^{(k)}(t), \bar{\zeta}_n^{(k)}(t)\big), \quad k=2,3, \tag{5.18}$$

where

$$J_{A_k}\big(\zeta_n^{(k)}(t), \bar{\zeta}_n^{(k)}(t)\big) = \frac{1}{2\pi}\int_{a_2}^{a_3}\log\left(\frac{\zeta-\zeta_n^{(k)}(t)}{\zeta-\bar{\zeta}_n^{(k)}(t)}\right)\left(\frac{(\zeta^2-a_3^2)(\zeta^2-a_2^2)}{(\zeta^2-a_4^2)(\zeta^2-a_1^2)}\right)^{1/2}\mathrm{d}\zeta. \tag{5.19}$$

The latter integrals may be asymptotically simplified by using the fact that only discrete vortices are localized at the corresponding edges. This implies the smallness of $|\zeta_n^{(k)} - \bar{\zeta}_n^{(k)}|$ and $|\zeta_n^{(k)} - a_k|$ (see Downie *et al.* 1988). Extracting the dominating asymptotic terms leads to

$$\left.\begin{aligned} J_{A_3} &= f_{A_3}\big(\zeta_n^{(3)} - \bar{\zeta}_n^{(3)}\big) + O\big(\big|\zeta_n^{(3)} - \bar{\zeta}_n^{(3)}\big|\big)\; O\big(\big|\zeta_n^{(3)} + a_3\big|\big) + o\big(\big|\zeta_n^{(3)} - \bar{\zeta}_n^{(3)}\big|\big),\\ J_{A_2} &= -f_{A_2}\big(\zeta_n^{(2)} - \bar{\zeta}_n^{(2)}\big) + O\big(\big|\zeta_n^{(2)} - \bar{\zeta}_n^{(2)}\big|\big)\; O\big(\big|\zeta_n^{(2)} + a_2\big|\big) + o\big(\big|\zeta_n^{(2)} - \bar{\zeta}_n^{(2)}\big|\big),\end{aligned}\right\} \tag{5.20}$$

where

$$\left.\begin{aligned} f_{A_2} &= \frac{1}{2\pi}\int_{-a_2}^{-a_3}\left(\frac{(a_2-\zeta)(\zeta^2-a_3^2)}{(\zeta^2-a_4^2)(a_1^2-\zeta^2)(\zeta+a_2)}\right)^{1/2}\mathrm{d}\zeta,\\ f_{A_3} &= \frac{1}{2\pi}\int_{-a_2}^{-a_3}\left(\frac{(\zeta-a_3)(\zeta^2-a_2^2)}{(a_3+\zeta)(\zeta^2-a_4^2)(\zeta^2-a_1^2)}\right)^{1/2}\mathrm{d}\zeta.\end{aligned}\right\} \tag{5.21}$$

As a consequence, the dominating terms for the vortex-induced forces are

$$F_v^{A_2} = \rho \mathrm{i}\frac{\mathrm{d}}{\mathrm{d}t}\left[\sum_{n=1}^{N_2}\Upsilon_n^{(2)}\big(\zeta_n^{(2)} - \bar{\zeta}_n^{(2)}\big)\right] f_{A_2}, \quad F_v^{A_3} = -\rho \mathrm{i}\frac{\mathrm{d}}{\mathrm{d}t}\left[\sum_{n=1}^{N_3}\Upsilon_n^{(3)}\big(\zeta_n^{(3)} - \bar{\zeta}_n^{(3)}\big)\right] f_{A_3}. \tag{5.22}$$

Following Downie *et al.* (1988) and using, to within the factors f_{A_k}, the similarity of the formulae (5.22) to (5.1) leads to

$$F_v^{A_3} = \tfrac{1}{2}\rho\big(\hat{U}^{(3)}\big)^2 L_{A_3} f_{A_3}\Psi_3(t), \qquad F_v^{A_2} = -\tfrac{1}{2}\rho\big(\hat{U}^{(2)}\big)^2 L_{A_2} f_{A_2}\Psi_2(t), \tag{5.23}$$

https://doi.org/10.1017/S002211200600440X Published online by Cambridge University Press

where

$$\Psi_k(t) = \bar{a}\sin(\sigma t + \theta_{A_k})|\sin(\sigma t + \theta_{A_k})| + \bar{b}\cos(\sigma t + \theta_{A_k}), \quad k = 2, 3.$$

Using the expressions (3.35) for the phase lags $\theta_{A_k}, k = 2, 3$, in $\Psi_k(t)$ the resulting vertical force on the side hulls reads

$$F_v = 2\big(F_v^{A_2} + F_v^{A_3}\big) = 3\rho\sigma^2 L_1^{8/3}\gamma^2$$
$$\times \Big[L_{A_3}^{1/3} f_{A_3}\big(\big(\alpha_1^{(2,1)}\big)^2 + \big(\alpha_1^{(2,2)}\big)^2\big)\Psi_3(t) - L_{A_2}^{1/3} f_{A_2}\big(\big(\alpha_1^{(1,1)}\big)^2 + \big(\alpha_1^{(1,2)}\big)^2\big)\Psi_2(t)\Big]. \quad (5.24)$$

The result depends on the frequency parameter Λ and the geometric parameters h, B and d.

The implementation of the formula (5.24) derived via the local vortex model was directly validated by considering the limiting case of a facing square in infinite fluid. This was achieved by letting the non-dimensional frequency be high, so that the free-surface condition approaches zero velocity potential on the mean free surface. Further, the relative distance $L_1/\bar{B}$ between the hulls and the relative water depth h/d were made sufficiently large to avoid a hull-interaction effect. The ambient flows at $\bar{A}_2$ and $\bar{A}_3$ become axis-symmetric (relative to the centre of the hull) and, therefore, $|\theta_{A_2} - \theta_{A_3}| \to \pi$ and $\Psi_3 \to -\Psi_2$ in (5.24). Introducing a double body consisting of the submerged part of the side-hull and its image about the free surface allows us then to relate our results to a facing square in infinite fluid. Our predicted drag coefficient for a single hull approached the value 1.735, which is in good agreement with the experimental drag coefficient of 1.6 reported by Graham (1977) for a low Keulegan–Carpenter number.

5.4. *Effect of vortex shedding*

5.4.1. *Vortex-induced work*

In order to estimate the vortex-induced effect on sloshing in the moonpool, one can calculate the time-averaged work of the vortex-induced vertical force F_v per cycle. It is defined as

$$\langle A_v\rangle = \frac{\sigma}{2\pi}\int_0^{2\pi/\sigma} F_v(t)\eta_{3a}\sigma\sin\sigma t\,\mathrm{d}t, \quad (5.25)$$

where the force is determined by (5.24). Direct calculations give

$$\langle A_v\rangle = 2\rho L_1^4\sigma^3\epsilon^2\left[\frac{1}{\epsilon}\left(W_{A_3}\left(\frac{4\bar{a}}{3\pi}\alpha_1^{(2,2)} - \frac{\bar{b}}{2}\alpha_1^{(2,1)}\right)\sqrt{\big(\alpha_1^{(2,1)}\big)^2 + \big(\alpha_1^{(2,2)}\big)^2}\right.\right.$$
$$\left.\left. - W_{A_2}\left(\frac{4\bar{a}}{3\pi}\alpha_1^{(1,2)} - \frac{\bar{b}}{2}\alpha_1^{(1,1)}\right)\sqrt{\big(\alpha_1^{(1,1)}\big)^2 + \big(\alpha_1^{(1,2)}\big)^2}\right)\right]$$
$$= 2\rho L_1^4\sigma^3\epsilon^2[\epsilon\mathscr{I}_v], \quad (5.26)$$

where the non-dimensional 'weight coefficients' caused by the geometry of the moonpool and the depth h are

$$W_{A_k} = \frac{3\gamma^2}{2}\left(\frac{L_{A_k}}{L_1}\right)^{1/3} f_{A_k}, \quad k = 2, 3.$$

The expression in the square brackets of (5.26) is non-dimensional and, due to linear theory, proportional to ϵ. The averaged non-dimensional work $\langle A_v\rangle$ due to vortex shedding is, therefore, of order ϵ^3. This is in contrast with the pure second-order expression (4.13), which computes the time-averaged total energy within the

https://doi.org/10.1017/S002211200600440X Published online by Cambridge University Press

framework of the linear inviscid theory. An important finding is the fact that the phase lags θ_{A_k} of the ambient flows at $\bar{A}_k$ expressed via $\alpha_1^{(i,j)}$ in (5.26) may cause either a drag or a thrust on the body. Because the weight coefficients W_{A_k} are proportional to γ^2 defined by (3.34) and because $\gamma \to \infty$ as $h - d \to 0$, while L_{A_k} and f_{A_k} do not depend on the fluid depth h, the work increases as $h \to d$ (shallow-water conditions).

5.4.2. *Energy balance*

Modifying the energy balance (4.13) to include the vortex-shedding work gives

$$\mathscr{I}_i + \epsilon \mathscr{I}_v = \frac{B_{33}}{2\sqrt{\Lambda}} + \epsilon \mathscr{I}_v = \mathscr{I}_o, \tag{5.27}$$

where $\mathscr{I}_i, \mathscr{I}_v$ and $\mathscr{I}_o$ are $O(1)$ unless $\Lambda \to 0$. This analysis disregards the effect of shear forces on the body as well as the viscous dissipation of energy in the fluid domain (Maisondieu *et al.* 2001; Molin 2004). Our earlier energy balance $\mathscr{I}_i = \mathscr{I}_o$ can be considered as a zero-order approximation in the limit $\epsilon \to 0$. Using ϵ as a small perturbation in (5.27), one can estimate the influence of vortex shedding on the outgoing wave amplitude. Indeed, utilizing (4.14), we can write down

$$\frac{P_a^*}{\epsilon} = \sqrt{\frac{2\mathscr{K} \sinh^2 \mathscr{K} h}{N_0} \left(\frac{B_{33}}{2\sqrt{\Lambda}} + \epsilon \mathscr{I}_v \right)}, \tag{5.28}$$

where P_a^* is the perturbed value of P_a, (4.3).

Further, because the zero-added mass A_{33} also occurs in a small vicinity of the resonant frequency Λ_*, the drift of this zero may also influence the shift of the maximum response. The corrected dimensional added mass may be computed as

$$\bar{A}_{33}^* = 2\rho L_1 \left(A_{33} - \frac{2\pi/\sigma \displaystyle\int_0^{2\pi/\sigma} F_v \cos \sigma t \, \mathrm{d}t}{2\rho L_1^3 \sigma^2 \epsilon} \right) = 2\rho L_1^2 (A_{33} + \epsilon \mathscr{J})_v, \tag{5.29}$$

where A_{33} is the non-dimensional added mass defined in § 4.2.3 and

$$\begin{aligned} \mathscr{J}_v = -\frac{1}{\epsilon^2} \Bigg[& W_{A_3} \left(\frac{4\bar{a}}{3\pi} \alpha_1^{(2,1)} + \frac{\bar{b}}{2} \alpha_1^{(2,2)} \right) \sqrt{\left(\alpha_1^{(2,1)}\right)^2 + \left(\alpha_1^{(2,2)}\right)^2} \\ & - W_{A_2} \left(\frac{4\bar{a}}{3\pi} \alpha_1^{(1,1)} + \frac{\bar{b}}{2} \alpha_1^{(1,2)} \right) \sqrt{\left(\alpha_1^{(1,1)}\right)^2 + \left(\alpha_1^{(1,2)}\right)^2} \Bigg] \end{aligned} \tag{5.30}$$

with $\mathscr{J}_v = O(1)$.

5.4.3. *Vortex-shedding effect on outgoing wave amplitude and added mass*

Our local vortex method cannot predict the direct consequence of vortex shedding on the moonpool elevation. However, as shown in previous paragraph, we can study the global conservation of energy and relate this to the far-field wave elevations. For example, employing the formulae (5.28) and (5.29) makes it possible to evaluate the effect of vortex shedding on the outgoing wave amplitude and the added mass in a neighbourhood of the resonant frequency Λ_* for experimental cases 1–3. Figure 11 shows that this influence is small. This is especially true for a small vicinity of Λ_*, at which the discrepancies between the experimental data and the linear inviscid prediction in figures 6(*c*) and 7(*c*) are substantial. A consequence is that a jump-like behaviour of the response amplitudes in figures 6(*c*), 7(*c*) and 8(*a*) for $\Lambda < \Lambda_*$

https://doi.org/10.1017/S002211200600440X Published online by Cambridge University Press

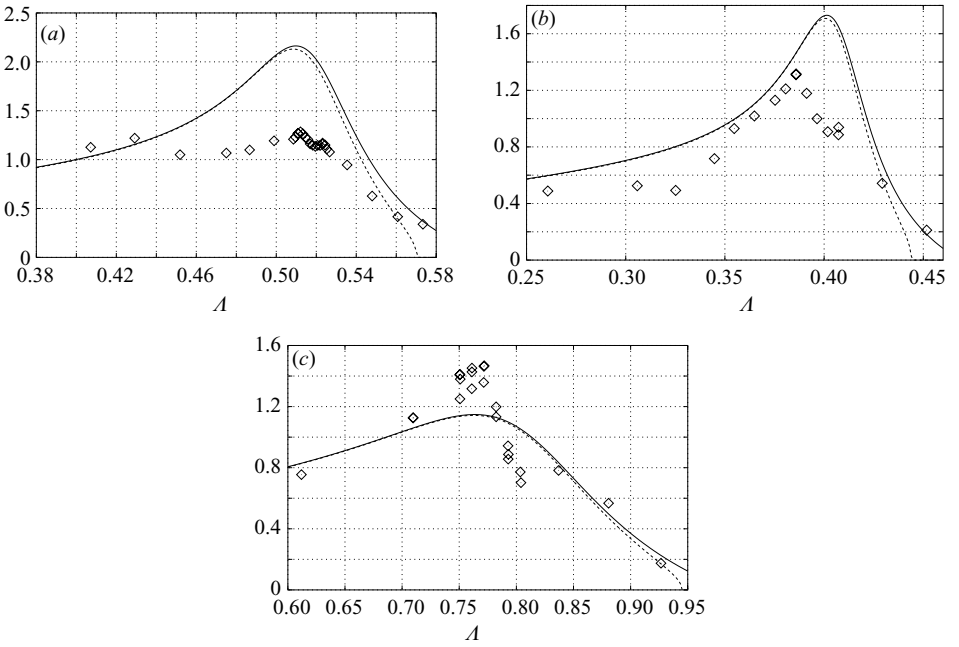


FIGURE 11. The dimensionless outgoing wave amplitude (scaled by the forcing amplitude) due to potential theory (solid line) and modified by the vortex shedding computed by (5.28). Panels (*a*)–(*c*) correspond to cases 1–3 with larger forcing amplitudes, respectively. The theoretical results may be compared with experimental measurements of the far-field amplitudes (symbols) from figures 6(*c*), 7(*c*) and 8(*d*).

cannot be explained by vortex shedding. Moreover, if vortex shedding should cause a damping, we cannot explain the fact that the experimental wave elevation in case 3 (figures 11*c* and 8*d*) is larger than in our linear theory.

Our procedure for computing the vorticity-perturbed outgoing wave amplitude fails in the neighbourhood of the points where the damping coefficient B_{33} vanishes (see figures 6(*f*), 7(*f*) and 8(*d*)). At these points, the outgoing wave amplitude P_a/ϵ computed by inviscid potential theory is small and, therefore, comparable with the ϵ-contribution in (5.28). Because vortex shedding causes a thrust on the body, the expression under the square root of (5.28) can then give a small negative value. In figures 11(*a–c*), we simply suppose the corrected elevations at the far field to be equal to zero.

The principal factor causing the very small influence of flow separation in the experimental cases is that the model tests were done with a small forcing amplitude, so that the second-order quantity due to the vortex-induced force gives a relatively small contribution. The vortex-induced contribution would be larger with increasing ϵ as well as with increasing non-dimensional B and decreasing $h - d$.

6. Concluding remarks

The primary purpose of this paper was to create an analytically oriented method which accurately predicts linear piston-like sloshing in a moonpool and can be adopted as a basis for nonlinear analytical studies. These studies suggest the methodology of Faltinsen *et al.* (2000) and Faltinsen, Rognebakke & Timokha (2003), developed for

https://doi.org/10.1017/S002211200600440X Published online by Cambridge University Press

the sloshing of a contained fluid, in which the semi-analytical linear solution plays the role of a functional set similar to the natural modes of the classical sloshing problem. For physical clarity and to avoid the mathematical difficulties that arise for moonpools of complex shape, the paper has focused on the mathematically simplest situation, i.e. the two-dimensional moonpool of a catamaran consisting of two rectangular hulls performing heave motions with a small amplitude. With the understanding that the principal mathematical and numerical difficulties are caused by the singular behaviour of the velocity potential at the corner points of the hulls, we reduced the original problem to a system of integral equations defined on the transmission lines which intersect the corners. A Galerkin projective scheme uses a singular basis, which correctly handles the above mentioned singularities and makes it possible to quantify the vortex-shedding effect by the discrete-vortex method of Graham (1980). A series of numerical experiments were performed to show that the semi-analytical method guarantees a high precision in computing the resonant frequencies (at which the maximum piston-like resonant amplitude is expected) and the free-surface amplitudes in both the moonpool and the far field. These showed a maximum 10^{-7} relative error for all the cases considered and, as a consequence, any discrepancy between the experiments and the theory cannot be related to insufficient numerical precision.

New model tests were carefully carried out to ensure high-precision measurements. The forced harmonic heave motions of a two-dimensional catamaran consisting of two equal rectangular side-hulls were considered. Comparing the measured responses for repeated tests with the same forcing parameters evaluated the random uncertainty error to be less than 3%.

The linear inviscid results were compared with the experimental data. The comparison between the experimental findings and the linear-theory results focused first on evaluation of the experimental resonance frequencies (at which the maximum piston-like amplitude is measured) and their theoretical predictions. These are in good agreement, so that the discrepancy is practically invisible on the corresponding graphs. Molin's formula, which was also used in the comparative analysis, gives larger values and only qualitative agreement. Furthermore, the comparative analysis deals with steady-state piston-like wave amplitudes inside the moonpool (taking averaged amplitudes over the moonpool width) as well as with wave elevations at wave probes located far from the piercing structure. In general, satisfactory quantitative agreement with experiment is shown, especially for the experimental series with lower forcing amplitudes. However, the latter quantitative theoretical results do not reflect some features of the experimentally established response curves, which, we believe, are caused by nonlinearities and, in part, damping. This is most evident for the piston-like amplitude.

In view of the results of Maisondieu *et al.* (2001) and Molin *et al.* (2002) for free oscillations in the moonpool, vortex shedding at the moonpool edges may cause substantial damping of the moonpool motion and therefore contribute to the discrepancy. The present paper generalizes the results by Graham (1980) and Downie *et al.* (1988) on the discrete vortex method for the studied case of steady-state forced waves. On the basis of these results, formulae for the vortex-induced vertical force and averaged work were derived. These are simple expressions in terms of the coefficients of the singular function from the structured Galerkin basis of the linear solution without vortex shedding. Computations showed that vortex shedding gives a small contribution to the damping coefficient and the amplitude of the outgoing waves. This confirms that vortex shedding itself cannot explain the discrepancy between theory

https://doi.org/10.1017/S002211200600440X Published online by Cambridge University Press

and experiment for the experimental cases considered. The reason is the relatively small forcing amplitudes and the quadratic velocity dependence of the vortex-induced forces.

Although the second-order effect of flow separation does not give a significant contribution in the cases studied, the free-surface nonlinearity associated with potential-flow effects may be important. Our basis for speculating about nonlinearities is our extensive sloshing studies and the fact that the moonpool elevation is not of the same order of magnitude as the forcing amplitude. That means differences in the ordering of terms should be made. The importance of nonlinearities is also confirmed explicitly by time recordings of the wave elevation, which highlight the contribution of higher harmonics in the steady-state regimes. Further, the importance of nonlinearity follows from the nonlinear analysis by Vinje (1991) (for a narrow moonpool) and an equivalent mechanical model of a moonpool by Miles (2004) and Hirata & Craik (2003). These detect a Duffing-like behaviour leading in particular to $O(\epsilon^{2/3})$ shifts in the maximum response. These shifts are qualitatively consistent with what was established in our model tests. Detailed theoretical studies of the nonlinear features of piston-like sloshing are planned in the future.

The practical help by Fredrik Dukan in the experimental part of this work was appreciated. The authors thank Professor J. M. R. Graham for very useful discussions of vortex shedding in the case studied.

REFERENCES

Aubin, J.-P. 1972 *Approximation of Elliptic Boundary-Value Problems*. John Wiley & Sons.

Bai, K. J. & Yeung, R. W. 1974 Numerical solutions to free-surface flow problems. *Proc. Tenth Symposium on Naval Hydrodynamics: Hydrodynamics of Safety Fundamental Hydrodynamics, June, 24–28, 1974, Cambridge, MA* (ed. R. D. Cooper & S. W. Doroff). ACR-204, pp. 609–647. Office of Naval Research-Department of Navy, Arlington, VA.

Courant, R. & Hilbert, D. 1953 *Methods of Mathematical Physics, Volume 1*. Interscience Publishers.

Downie, M. J., Bearman, P. W. & Graham, J. M. R. 1988 Effect of vortex shedding on the coupled roll response of bodies in waves. *J. Fluid Mech.* **189**, 243–264.

Drobyshevski, Y. 2004 Hydrodynamic coefficients of a two-dimensional, truncated rectangular floating structure in shallow water. *Ocean Engng* **31**, 305–341.

Erdélyi, T. & Johnson, W. B. 2001 The "full Müntz theorem" in $L_p[0, 1]$ for $0 < p < \infty$. *J. Anal. Maths* **84**, 145–172.

Faltinsen, O. M. 1974 A nonlinear theory of sloshing in rectangular tanks. *J. Ship Res.* **18**, 224–241.

Faltinsen, O. M. 1990 *Sea Loads on Ships and Offshore Structures*. Cambridge University Press.

Faltinsen, O. M., Rognebakke, O. F., Lukovsky, I. A. & Timokha, A. N. 2000 Multidimensional modal analysis of nonlinear sloshing in a rectangular tank with finite water depth. *J. Fluid Mech.* **407**, 201–234.

Faltinsen, O. M., Rognebakke, O. F. & Timokha, A. N. 2003 Resonant three-dimensional nonlinear sloshing in a square base basin. *J. Fluid Mech.* **487**, 1–42.

Faltinsen, O. M., Rognebakke, O. F. & Timokha, A. N. 2006 Transient and steady-state amplitudes of resonant three-dimensional sloshing in a square base tank with a finite fluid depth. *Phys. Fluids* **18**, 012103.

Faltinsen, O. M. & Timokha, A. N. 2001 Adaptive multimodal approach to nonlinear sloshing in a rectangular rank. *J. Fluid Mech.* **432**, 167–200.

Gavrilyuk, I. P., Lukovsky, I. A., Trotsenko, V. A. & Timokha, A. N. 2006 Sloshing in a vertical circular cylindrical tank with an annular baffle. Part 1. Linear fundamental solutions. *J. Engng Maths* **54**, 71–88.

Graham, J. M. R. 1977 Vortex shedding from sharp edges. *Imp. Coll. Aero. London, Rep.* 77-06.

https://doi.org/10.1017/S002211200600440X Published online by Cambridge University Press

Graham, J. M. R. 1980 The forces on sharp-edged cylinders in oscillatory flow at low Keulegan-Carpenter numbers. *J. Fluid Mech.* **97**, 331–346.

Grisvard, P. 1985 *Elliptic Problems in Nonsmooth Domains*. Pitman.

Hirata, K. & Craik, A. D. D. 2003 Nonlinear oscillations in three-armed tubes. *Eur. J. Mech.* B/*Fluids* **22**, 328.

Kan, M. 1977 The added mass coefficient of a cylinder oscillating in shallow water in the limit $K \to 0$ and $K \to \infty$. *Papers of Ship Research Institute*, No. 52, 21pp.

Kuznetsov, N., Maz'ya, V. & Vainberg, B. 2002 *Linear Water Waves. A Mathematical approach* Cambridge University Press.

Kuznetsov, N., McIver, P. & Linton, C. M. 2001 On uniqueness and trapped modes in the water-wave problem for vertical barriers. *Wave Motion* **33**, 283–307.

Lewis, R. I. 1991 *Vortex Element Methods for Fluid Dynamic Analysis of Engineering Systems*. Cambridge University Press.

Maisondieu, C., Molin, B., Kimmoun, O. & Gentaz, L. 2001 Simulation bidmensionnelle des écoulements dans une baie de forage: étude des modes de résonance et des amortissements. *Actes des Huitièmes Journées de l'Hydrodynamique, Nantes*, pp. 251–264 (in French).

Mavrakos, S. A. 2004 Hydrodynamic coefficients in heave of two concentric surface-piercing truncated circular cylinders. *Appl. Ocean Res.* **26**, 84–97.

McIver, M. 1996 An example of non-uniqueness in the two-dimensional linear water wave problem. *J. Fluid Mech.* **315**, 257–266.

McIver, P. 2005 Complex resonances in the water-wave problem for a floating structure. *J. Fluid Mech.* **536**, 423–443.

McIver, P. & Linton, C. M. 1991 The added mass of bodies heaving at low frequency in water of finite depth. *Appl. Ocean Res.* **13**, 12–17.

McIver, P., McIver, M. & Zhang, J. 2003 Excitation of trapped water waves by the forced motion of structures. *J. Fluid Mech.* **494**, 141–162.

Miles, J. 2004 Slow nonlinear oscillations in a circular well. *J. Fluid Mech.* **498**, 403–406.

Molin, B. 2001 On the piston and sloshing modes in moonpools. *J. Fluid Mech.* **430**, 27–50.

Molin, B. 2004 On the frictional damping in roll of ship sections. *Intl Shipbuild. Progr.* **51**, No. 1, 59–85.

Molin, B., Remy, F., Kimmoun, O. & Stassen, Y. 2002 Experimental study of the wave propagation and decay in a channel through a rigid ice-sheet. *Appl. Ocean Res.* **24**, 247–260.

Müntz, C. 1914 *Über den Approximationsatz von Weierstrass*. H.A. Schwartz Festschift, Berlin.

Newman, J. N. 1977 *Marine Hydrodynamics*. MIT Press.

Newman, J. N. 1999 Radiation and diffraction analysis of the McIver toroid. *J. Engng Maths* **35**, 135–147.

Ohkusu, M. 1970 On the motions of multihull ships in waves. *Report of Research Institute of Applied Mechanics, Kyushu University*, V. XVIII, N 60.

Ohkusu, M. & Takaki, M. 1971 On the motions of multihull ships in waves (II). *Report of Research Institute of Applied Mechanics, Kyushu University*, V. XIX, N 62.

Porter, R. & Evans, D. V. 1995 Complementary approximations to wave scattering by vertical barriers. *J. Fluid Mech.* **294**, 155–180.

Sarpkaya, T. & Isaacson, M. 1981 *Mechanics of Wave Forces on Offshore Structures*. Van Nostrand Reinhold.

Singh, S. 1979 Forces on bodies in oscillatory flow. PhD thesis, University of London.

Vinje, T. 1991 An approach to non-linear solution of the oscillating water column. *Appl. Ocean Res.* **13**, 18–36.

Williams, A. N. & Abul-Azm, A. G. 1997 Dual pontoon floating breakwater. *Ocean Engng* **24**, 465–478.

https://doi.org/10.1017/S002211200600440X Published online by Cambridge University Press